# PROX1 loss in adult mouse Schlemm's canal causes permanent ocular hypertension

Sofia L. Ochoa[a], Hoi Lam Li[b], Hyeohn Kim[a], Zihang Yan[a], Natalia C. Mendonca[a], Pan Liu[c], Hyunjoo J Lee[d], Michael P. Vincent[a], Sultan Almunif[a], Hao F. Zhang[a,e], Haiyan Gong[b], *&Evan A. Scott[a, f], *&Mark Johnson[a, e] and *&Benjamin R. Thomson[a, e, g]

[a]Department of Biomedical Engineering, Northwestern University, Evanston, Il

[b]Department of Ophthalmology and Department of Anatomy and Neurobiology, Boston University School of Medicine, Boston, MA

[c]Section of Nephrology and Hypertension, Northwestern University Feinberg School of Medicine, Chicago, IL

[d]Massachusetts Eye and Ear, Boston, Ma and Harvard Medical School, Cambridge, MA.

[e]Department of Ophthalmology, Northwestern University Feinberg School of Medicine, Chicago, IL

[f]Department of Biomedical Engineering, NanoSTAR Institute, University of Virginia School of Medicine, Charlottesville, VA

[g]Feinberg Cardiovascular and Renal Research Inst. Northwestern University Feinberg School of Medicine, Chicago, IL

*Contributed equally

&Please address correspondence to:

Benjamin R Thomson
benjamin.thomson@northwestern.edu
Northwestern University Feinberg Cardiovascular and Renal Research
SQBRC 8-407 302 E Huron St, Chicago, IL, 60611

Mark Johnson
m-johnson2@northwestern.edu
Northwestern University Department of Biomedical Engineering
Tech E3782145 Sheridan Rd, Evanston IL, 60208

Evan A Scott
der4yt@virginia.edu
University of Virginia, School of Medicine and Engineering
Carter Harrison Research Building, MR6-B523
345 Crispell Dr. Charlottesville VA, 22903

Running title: Prox1 deletion caused ocular hypertension

Word Count: 11,008. Abstract: 197

35 **COMPETING INTERESTS**

36 EAS, MJ, BRT, SLO and NCM have submitted a patent application related to therapeutic
37 targeting of PROX1 in ocular hypertension and glaucoma. EAS, MJ and MPV have applied for a
38 patent related to PEG-b-PPS nanocarrier-based glaucoma therapies, and EAS holds and has
39 applied for patents related to PEG-b-PPS-based therapies for other diseases. In addition, EAS is
40 the CEO and founder of SNC Therapeutics Inc., a startup company focused on developing a gene
41 delivery vehicle based upon the PEG-PPS platform. HFZ holds patents on visible light OCT-
42 related technologies and is a founder of Opticent Health. Other authors declare no competing
43 interests.

**ABSTRACT**

Glaucoma is associated with ocular hypertension, and lowering intraocular pressure is the primary objective of current therapies. Recent studies have established a key role for Schlemm's canal endothelium in this pressure increase and have shown that it has a unique, lymphatic-like hybrid phenotype characterized by expression of the lymphatic transcription factor PROX1. However, the functional importance of this hybrid phenotype in the adult canal remains unclear, as long-term studies have been limited by systemic requirements for lymphatic gene expression and a lack of Schlemm's canal–specific animal models. Here, we designed and validated a strategy using 4OH-tamoxifen-loaded nanocarriers to generate targeted, Schlemm's canal-specific *Prox1* knockout mice that specifically lacked lymphatic characteristics in the canal endothelium. Within four weeks, intraocular pressure was significantly elevated, and ocular hypertension was maintained for at least 24 weeks. Unlike lymphatic vessels, which degenerate following *Prox1* deletion, Schlemm's canal persisted but reverted to a less functional vein-like phenotype with no change in size or morphology. Together, these findings demonstrate the utility of nanocarrier-mediated tamoxifen delivery and establish the importance of the Schlemm's canal lymphatic-like phenotype in intraocular pressure regulation, providing targets for future glaucoma therapies and a mouse model of adult-onset ocular hypertension.

62 **INTRODUCTION**

63 Glaucoma is a leading cause of vision loss worldwide, affecting an estimated 64 million people
64 and leaving 3.6 million blind (1). While death of retinal ganglion cells is directly responsible for
65 the vision loss, elevated intraocular pressure (IOP) is the only modifiable risk factor for
66 development and progression of primary open-angle glaucoma (POAG), the most prevalent form
67 of the disease. Pharmacological IOP reduction slows progression and lowers glaucoma risk (2,
68 3). However, even on maximal medical therapy, progressive visual field loss still occurs in some
69 patients, indicating current pharmacological treatments are not always sufficient and highlighting
70 the need for new therapeutic approaches (4, 5). This is likely due to the (i) inability of current
71 therapeutics to continuously keep IOP low enough to protect the optic nerve and (ii) lack of
72 treatments that directly address the underlying pathology causing ocular hypertension.

73 The aqueous humor flows through the anterior segment of the eye providing nutrition and
74 removing metabolic wastes and leaves the eye primarily through an outflow pathway comprised
75 of the trabecular meshwork and Schlemm's canal—a unique vessel adjacent to the iridocorneal
76 angle—and emptying into the collector channels and aqueous veins (6, 7). Resistance to flow
77 through this pathway generates IOP, and in glaucoma, this flow resistance is elevated, causing
78 ocular hypertension. A significant fraction of the total resistance is generated as aqueous humor
79 passes through the deeper regions of the trabecular meshwork and/or the basal lamina of
80 Schlemm's canal before entering the canal through pores in its endothelial inner wall. These
81 pores modulate outflow resistance (8) and their density is reduced in glaucoma (9, 10). It has
82 recently been reported that this decreased pore density is negatively correlated with increased
83 stiffness of the Schlemm's canal endothelium in glaucomatous eyes (11, 12). Thus, it is likely
84 that physical properties of Schlemm's canal cells themselves, and/or their underlying basal

85 lamina, play a central role in modulating resistance and IOP homeostasis (13). However, how
86 Schlemm's canal endothelial stiffness, pore number, and outflow resistance are regulated at the
87 molecular level, and how they might become dysregulated to increase resistance in POAG
88 remain topics of ongoing research.

89 Schlemm's canal is a unique vessel with characteristics of lymphatics, such as a discontinuous
90 basement membrane and basal to apical transendothelial flow, and those of a venule including a
91 continuous network of cell-cell junctions (14, 15). Like other hybrid vessels (16-20), Schlemm's
92 canal is derived from blood vascular endothelium and acquires a lymphatic-like phenotype
93 during development (21). However, how lymphatic characteristics impact function remains
94 unclear. Lymphatic capillaries are highly permeable as befits their function (22). While
95 Schlemm's canal endothelial cells lack the unique junctional morphology of lymphatic capillaries
96 (21, 23), the canal inner wall has one of the highest hydraulic conductivities of any endothelium
97 in the human body (24), suggesting lymphatic gene expression may facilitate increased
98 permeability.

99 The lymphatic-like "hybrid" vascular phenotype of Schlemm's canal cells is defined at the
100 molecular level by the lymphatic master transcription factor PROX1 (21, 25-27). Developmental
101 deletion or blockade of PROX1 or the typically lymphatic receptor tyrosine kinase FLT4 (also
102 known as VEGFR3) results in an attenuated canal with disorganized morphology (21, 25, 28,
103 29). However, it is unknown whether PROX1 regulates the same transcriptional targets in the
104 canal as in lymphatic vessels, or if it has a continuing role in the adult eye. Other developmental
105 pathways, including VEGFA-VEGFR2 and ANGPT1-TEK, regulate IOP homeostasis throughout
106 life (21, 30-33) and lymphatic gene expression is maintained in the mature Schlemm's canal,
107 supporting continued importance (21, 25, 29). As the elevated pressure characteristic of

108 glaucoma is associated with a loss of tissue permeability, we hypothesized that this might be
109 related to the lymphatic character of the Schlemm's canal endothelium and its regulation by
110 PROX1. Although a previous report did not observe IOP elevation 2 weeks after endothelial
111 *Prox1* deletion in adult mice (28), these animals died within 3 weeks, leaving it unknown if
112 lymphatic phenotypes were dispensable in the adult canal or if dysfunction developed over a
113 longer timeline, consistent with human glaucoma (28).

114 We have previously developed a highly specific nanocarrier platform comprised of the
115 amphiphilic block copolymer poly(ethylene glycol)-*b*-poly(propylene sulfide) (PEG-*b*-PPS) (34)
116 for targeted drug delivery to the Schlemm's canal endothelium (35, 36). Here, we adapted the
117 platform to deliver 4-OH-Tamoxifen (4OHT), a tamoxifen metabolite that is commonly used to
118 induce recombination in CreERT2-expressing mouse strains (37). By delivering 4OHT
119 nanocarriers to a single eye, this system allowed us to induce deletion within an individual
120 Schlemm's canal and obtain same-animal controls by injecting empty nanocarriers in
121 contralateral eyes.

122 Following validation, targeted 4OHT-loaded nanocarriers were used to ablate Schlemm's canal
123 lymphatic phenotypes via deletion of *Prox1* from adult Schlemm's canal, bypassing lethal
124 systemic phenotypes. Within 4 weeks, we observed specific, reproducible IOP elevation that
125 persisted throughout life, thus identifying a critical role for PROX1 and Schlemm's canal's
126 lymphatic phenotype in IOP homeostasis while also generating an adult-onset model of ocular
127 hypertension.

128

129 **RESULTS**

130 *Schlemm's canal endothelial cells have a hybrid lymphatic-like phenotype that is mediated in*
131 *mouse and human by PROX1*

132 The hybrid identity of Schlemm's canal endothelial cells has been reported in the mouse eye at
133 both mRNA and protein levels (21, 25, 27, 29, 38, 39). In the human eye, while lymphatic gene
134 expression has been identified by single-cell RNA sequencing (38, 40, 41), it has been less well
135 characterized at the protein level and conflicting reports have been published (25, 42). To verify
136 the lymphatic identity of this endothelium and determine if it is regulated by PROX1, we
137 performed immunostaining of mouse and human canals. Confocal microscopy of mouse eye
138 whole mounts (Figure 1A) and cryosections from human corneal rim tissue obtained after
139 transplant surgery (Figure 1B) confirmed that the canal of both species expressed lymphatic
140 markers PROX1 and FLT4, but not LYVE1 (Supplemental Figure 1) confirming their hybrid
141 identity. PROX1 expression was negatively correlated with donor age (Supplemental Figure 2
142 A), consistent with reported findings in the mouse eye (28).

143 As PROX1 directly regulates the fate of lymphatic endothelial cells, we speculated that it played
144 a similar role in Schlemm's canal. To test this directly, we treated primary human Schlemm's
145 canal cells with a previously validated siRNA targeting *PROX1 (43)*. 72 h after treatment, real-
146 time rtPCR was used to confirm *PROX1* knockdown (Figure 1C). Expression of *CCL21* and
147 *FLT4*, additional lymphatic markers expressed by Schlemm's canal endothelial cells (Figure 1C-
148 E) (25), were also suppressed, suggesting loss of PROX1 resulted in a general reduction of
149 lymphatic gene expression. Expression of *TEK*, an endothelial receptor tyrosine kinase expressed
150 in both blood and lymphatic endothelial cells, was unchanged (Figure 1C). RNA sequencing
151 revealed downregulation of additional canal-expressed lymphatic genes in si*PROX1*-treated
152 cells, including *ITGA9* and *GATA2* (Figure 1F, Supplemental dataset 1). In contrast, a subset of

153 blood-endothelial-specific genes including *ICAM1*, *VCAM1* and *PTPRB* were upregulated.
154 Together these findings suggested that, as in lymphatic endothelial cells (44), the lymphatic
155 transcriptional program in Schlemm's canal endothelial cells was mediated by PROX1.

156 To understand the role of PROX1 in mediating the Schlemm's canal hybrid phenotype *in vivo*,
157 we next turned to an endothelial-specific *Prox1* knockout mouse model (45). *Prox1*$^{flox/flox}$; *Cdh5-*
158 CreERT2 mice were generated and induced with tamoxifen at 8 weeks of age to obtain animals
159 lacking *Prox1* in all endothelial cells, including those in Schlemm's canal (*Prox1*ΔEC). Four
160 weeks after induction, immunostaining revealed robust PROX1 ablation, although some
161 mosaicism was observed and occasional endothelial cells retained PROX1 (Figure 1G, quantified
162 in H). FLT4 staining was also reduced, consistent with our *in vitro* data and the well-known role
163 of PROX1 in regulating FLT4 expression in lymphatic endothelial cells (44). IOP measurement
164 by rebound tonometry (Figure 1I), revealed normal IOP, and no change in Schlemm's canal size
165 was observed when measured using immunofluorescence confocal microscopy in canal whole
166 mounts (Figure 1J).

167 Lack of IOP elevation two weeks after whole endothelial *Prox1* deletion has been previously
168 reported (28) and, as in those reports, we were unable to track the IOP of *Prox1*ΔEC mice
169 beyond 4 weeks due to intestinal hemorrhage and lethality, likely caused by the role of lymphatic
170 vessels in maintaining the gut epithelium (28, 46). While these data confirmed PROX1 regulated
171 Schlemm's canal's lymphatic gene expression, we remained skeptical that the hybrid identity was
172 unnecessary for IOP homeostasis—especially as the decrease in PROX1 expression with age in
173 mice (28) and humans (Supplemental Figure 2A) is consistent with an age-related increase in
174 outflow resistance that occurs in humans (47). Thus, we speculated that the short survival time
175 of *Prox1*ΔEC mice might be insufficient to observe an IOP phenotype, or that whole-endothelial

176 *Prox1* deletion caused confounding phenotypes that lowered IOP or prevented accurate
177 tonometric measurements.

178 To bypass systemic phenotypes, we determined that Schlemm's canal-specific deletion would be
179 required. However, no canal-specific Cre-expressing mouse line has been described,
180 necessitating the development of a new approach. We therefore employed the PEG-*b*-PPS
181 nanocarrier delivery system previously developed by our group in order to selectively deliver the
182 active metabolite 4OHT directly to Schlemm's canal endothelial cells of *Prox1*$^{flox/flox}$; *Cdh5*-
183 CreERT2 mice to induce Schlemm's canal-specific cre-mediated recombination.

184

185 *Targeted 4OH-tamoxifen nanocarriers specifically induce gene deletion in Schlemm's canal*
186 *endothelial cells*

187 Modifying a PEG-*b*-PPS delivery system that was previously developed by our group (34-36),
188 we designed a targeted nanocarrier system to selectively deliver 4OHT to Schlemm's canal
189 endothelial cells *in vivo* to achieve SC-specific, Cre-mediated gene deletion. Combined with
190 endothelial-specific expression of Cre-ERT2 in *Cdh5*-CreERT2 mice, we predicted that this
191 system would allow robust, two-level selectivity for the Schlemm's canal endothelium. Micellar
192 nanocarriers were generated, loaded with 4OHT, and decorated with VEGFC-derived peptide-
193 lipid targeting constructs (PG48), which we have previously optimized for FLT4 binding and
194 selective delivery to the Schlemm's canal endothelium (Figure 2A) (35, 36). Unlike
195 unmetabolized tamoxifen that must circulate for processing by cytochrome P450 in the liver
196 (48), 4OHT is active immediately in cells where it is delivered, making it the optimal cargo for
197 this application. 4OHT nanocarriers exhibited a stable monodisperse particle size distribution

198 (PDI ≤ 0.2) with a diameter of 17-22 nm when assessed by cryo-electron microscopy and
199 dynamic light scattering (DLS; Figure 2B, Supplemental Figure 3A and Table 1). Zeta-potential
200 was determined by electrophoretic light scattering (ELS), indicating a neutral surface charge
201 (Table 1). Spherical morphology was confirmed by cryo-transmission electron microscopy
202 (Cryo-TEM; Figure 2B) and small angle x-ray scattering (SAXS; Figure 2C) and was unaffected
203 by addition of 4OHT and targeting peptides. Encapsulation efficiency of 4OHT was 47-54%
204 (Table 1) with a resulting concentration of 80-120 µg/mL encapsulated 4OHT in injectable
205 formulations. No cytotoxicity was observed in cultured HUVECs treated with nanocarrier
206 concentrations up to 2µM 4OHT (Supplemental Figure 3B). Validating the targeting approach,
207 flow cytometry demonstrated that VEGFC-derived targeting peptides increased uptake of DiI-
208 labeled nanocarriers by primary human Schlemm's canal cells but not in HUVECs, which do not
209 express FLT4 (Supplemental Figure 3C).

210

211 *4OH-tamoxifen nanocarriers specifically induce gene deletion in Schlemm's canal in vivo*

212 To determine if 4OHT nanocarriers could induce high-efficiency, Schlemm's canal–specific
213 recombination and whether FLT4 targeting was as effective in vivo as in our in vitro system, we
214 administered parallel intracameral injections of targeted and untargeted 4OHT nanocarriers to
215 eyes of *Rosa26*$^{mTmG}$; *Cdh5*-CreERT2 reporter mice (Figure 3A). Eyes were collected for analysis
216 seven days later. Although sporadic 4OHT-induced Cre-mediated recombination was observed in
217 eyes receiving untargeted, 4OHT-loaded nanocarriers, the majority of the endothelial cells
218 remained unrecombined, indicating low-efficiency uptake (Figure 3B). In contrast,
219 recombination efficiency was markedly increased in eyes treated with FLT4-targeted 4OHT
220 nanocarriers, confirming effectiveness of the targeting strategy (Figure 3B).



*Prox1 deletion caused ocular hypertension*

221 We next tested repeat nanocarrier injections as a tool to increase recombination efficiency
222 (Figure 3C). Following a second injection 24 h after the first, we observed nearly complete
223 labeling of the Schlemm's canal endothelium. Despite robust recombination within the eye
224 receiving 4OHT nanocarriers, no recombination was observed in Schlemm's canal of
225 contralateral eyes that received identical FLT4-targeted empty (blank) nanocarriers as a control
226 (Figure 3C), or within retinal or choroidal capillaries of either eye (Supplemental Figure 4),
227 confirming specificity of the targeting approach and lack of systemic recombination. Mosaic
228 recombination was seen in distal outflow vessels of eyes receiving 4OHT-loaded nanocarriers,
229 suggesting some nanocarriers flowed through the canal without uptake by Schlemm's canal
230 endothelium, and in limbal lymphatic capillaries, consistent with their known expression of
231 FLT4 (Supplemental Figure 5A and B). Outside of the eye, while we observed GFP expression in
232 some endothelial cells of the liver, kidney and lung (Supplemental Figure 6), recombination
233 levels were similar to those in untreated animals, indicating that recombination in these tissues
234 was due to leakiness of Cre activity and not off target nanocarrier delivery.

235

236 *Schlemm's canal-specific Prox1 deletion caused ocular hypertension in adult mice*

237 Following validation of targeted 4OHT nanocarriers, we examined the long-term role of PROX1
238 in maintaining IOP homeostasis. We generated cohorts of *Prox1*$^{flox/flox}$; *Cdh5*-CreERT2 mice with
239 Cre-negative littermate controls. At 8 weeks of age, Schlemm's canal-specific *Prox1* deletion was
240 induced in randomized eyes with Schlemm's canal targeted 4OHT nanocarriers. Contralateral
241 eyes received identical injections of targeted empty (blank) nanocarriers as a control (Figure 4A).
242 At baseline, we observed no difference in IOP between eyes ($\Delta IOP_{baseline}$ = 0.2±0.6 mmHg, p
243 >0.9), but beginning 4 weeks after induction, IOP in 4OHT-treated eyes was significantly

244 elevated in comparison with same-animal control eyes (Figure 4B and C, $\Delta IOP_{4wks} = 4.5 \pm 0.8$
245 mmHg, $p < 0.005$). No IOP difference was observed between eyes in Cre- littermates insensitive
246 to tamoxifen ($\Delta IOP_{4wks} = -0.6 \pm 0.5$ mmHg, $p > 0.9$). IOP remained elevated for 18 weeks, as long
247 as the animals were maintained. In an independent replication cohort, elevated IOP was observed
248 for 24 weeks, again as long as the animals were maintained (Supplemental Figure 7, $\Delta IOP_{24wks} =$
249 $4.4 \pm 1.3$ mmHg, $p < 0.001$). Surprisingly, given increased IOP and the central role of PROX1 in
250 Schlemm's canal development, *in vivo* visible light optical coherence tomography (vis-OCT)
251 imaging performed 12 weeks after induction revealed no difference in Schlemm's canal size or
252 morphology between PROX1 knockout and same animal contralateral control eyes (Figure 4D
253 and E, quantified in F).

254 Following longitudinal IOP measurements, enucleated eyes were stained and prepared for
255 immunofluorescent imaging (whole mounts) and for light and electron microscopy (cross-
256 sections). Compared to contralateral controls, confocal microscopy confirmed reduced PROX1
257 immunostaining in canals of targeted 4OHT nanocarrier-treated eyes (56±10.8% reduction, p
258 <0.001; Figure 4G, quantified in H). Schlemm's canal size, as measured by PECAM1-positive
259 immunofluorescence, was unchanged (Figure 4I). At 12 weeks of age, light microscopy in a
260 separate group of animals revealed no differences in gross canal morphology or geometric
261 parameters between *Prox1* knockout and contralateral control eyes (Figure 5A-D). Similarly,
262 when imaged using transmission electron microscopy (Figure 5E), we did not observe
263 differences in the morphology of Schlemm's canal inner wall or juxtacanalicular connective
264 tissue. Giant vacuoles were observed in the Schlemm's canal of both *Prox1* knockout and control
265 eyes.

266 These findings suggested that increased IOP seen following *Prox1* deletion was due to alterations
267 in outflow function of the targeted Schlemm's canal cells and/or in their communication and
268 interactions with neighboring cells or extracellular matrix, rather than canal degeneration or
269 gross morphological changes. Furthermore, they confirmed the efficacy of FLT4-targeted 4OHT
270 nanocarriers for gene deletion within Schlemm's canal and demonstrated that PROX1-mediated
271 lymphatic hybrid phenotypes were essential for IOP homeostasis.

272 In contrast to the long-term persistence of Schlemm's canal following *Prox1* deletion, we
273 observed a reduced number of limbal lymphatic capillaries in 4OHT nanocarrier-treated eyes,
274 which were targeted by our FLT4-based strategy in addition to Schlemm's canal (Supplemental
275 Figure 8), consistent with their requirement for ongoing PROX1 activity (44, 49). Normal
276 PROX1 expression was seen in remaining lymphatics, suggesting that deletion efficacy in these
277 vessels was lower than in Schlemm's canal—perhaps because the limbal lymphatics do not
278 connect to the anterior chamber and lacked a direct route for nanocarrier entry.
279

280 *Endothelial-specific Flt4 knockout mice induced as adults had normal IOP*

281 While PROX1 has many direct transcriptional targets, one of the best characterized is *Flt4*.
282 *PROX1* knockdown in cultured lymphatic endothelial cells (44) and in primary human
283 Schlemm's canal cells (Figure 1) led to reduction of *FLT4*, and *PROX1* overexpression drives
284 ectopic *FLT4* expression in blood vascular endothelial cells (44). In mouse lymphatic vessels,
285 *Prox1* deletion leads to loss of FLT4 and the lymphatic phenotype overall (50, 51). Accordingly,
286 as FLT4 is essential for Schlemm's canal development and its ligand VEGFC induces angiogenic
287 sprouting from the adult canal (25), we speculated FLT4 downregulation may be the cause of
288 IOP elevation in *Prox1* knockout eyes. Therefore, we generated endothelial-specific *Flt4*

289 knockout mice using *Cdh5*-CreERT2 (*Flt4*ΔEC), and induced deletion by tamoxifen injection at
290 8 weeks of age (Figure 6A).

291 Twenty weeks after tamoxifen administration, confocal microscopy revealed loss of FLT4
292 immunostaining from Schlemm's canal in *Flt4*ΔEC mice (Figure 6B, quantified in C) with no
293 change in PECAM1-positive Schlemm's canal size or morphology (Figure 6D). No difference in
294 IOP was observed between *Flt4*ΔEC mice and Cre negative control littermates (ΔIOP = 0.4
295 mmHg, $p > 0.7$; Figure 6E). These data indicated that, while FLT4 is essential for Schlemm's
296 canal development (25), it was dispensable in the adult canal and FLT4 downregulation was not
297 responsible for the IOP elevation seen in *Prox1*ΔSC eyes.

298

299 **DISCUSSION**

300 It has long been known (6, 7), that the ocular hypertension characteristic of POAG is due to
301 increased resistance to the flow of aqueous humor through the outflow pathway in the eye. While
302 cause of this increased resistance remains incompletely understood, several factors implicate the
303 inner wall region of Schlemm's canal of glaucomatous eyes including decreased pore density (9,
304 10), increased cellular (52) and tissue stiffness (12, 53), and increased pressure drop in this
305 region (12). As there is also evidence that Schlemm's canal endothelium modulates outflow
306 resistance and thereby IOP in the normal eye (8), here, we focused on how this modulation might
307 occur.

308 PROX1 is crucial for Schlemm's canal development, but its systemic importance within the
309 lymphatic endothelium has prevented long-term studies of its role in the adult eye and masked
310 any ongoing role in IOP regulation (28). Here, by deleting *Prox1* selectively from Schlemm's

311 canal endothelium, our targeted nanocarrier approach allowed us to study knockout eyes over a
312 longer period and revealed an unappreciated but essential role for PROX1 in IOP homeostasis.

313 Schlemm's canal originates through sprouting angiogenesis from blood-filled capillaries in the
314 limbal and iridocorneal angle regions of the eye (21, 25). PROX1 expression begins concurrently
315 with canal lumenization, and in turn initiates expression of FLT4 and other lymphatic markers.
316 The molecular identity of true lymphatic vessels is maintained by a signaling loop of PROX1
317 and FLT4 (44, 49). Without continuous PROX1 transcriptional activity, lymphatic endothelial
318 cells revert towards a venous phenotype and degenerate (49), consistent with the loss of limbal
319 lymphatic capillaries that we observed in *Prox1* knockout eyes. Conversely, while deletion of
320 *Prox1* from Schlemm's canal markedly increased IOP, we did not observe canal degeneration or
321 reduction in canal size over timelines up to 6 months.

322 Together, these findings suggested that the PROX1-mediated hybrid phenotype was essential for
323 IOP homeostasis, but that without PROX1, Schlemm's canal could indefinitely revert to a less
324 functional vein-like phenotype. This mirrors other PROX1-expressing hybrid vessels (20) and
325 suggests re-programming the Schlemm's canal endothelium to enhance or restore its functional
326 hybrid phenotype may be an effective long-term or permanent strategy for enhancing or restoring
327 outflow. We further showed relevance of this model to the human eye by confirming the presence
328 of PROX1 in human Schlemm's canal, as predicted by single cell RNA sequencing (38, 41) and
329 in agreement with the findings of Aspelund et al. (25) but contrary to the report of Birke et al.
330 (42).

331 While these findings established a clear connection between the hybrid phenotype and function,
332 the mechanistic link is still unclear. Lymphatic capillaries are less stiff (54) and more permeable
333 (22) than veins, characteristics central to the function of Schlemm's canal. This suggests that

334 elevated IOP in this model may be due to lowered permeability of the inner wall endothelial cells
335 following *Prox1* deletion. How these characteristics are regulated by PROX1 is unknown, but
336 our *in-vitro* studies provided clues. Following siRNA-mediated *PROX1* knockdown, expression
337 of *PTPRB,* the gene encoding the TEK and VE-Cadherin-regulating phosphatase VE-PTP, was
338 increased. *Ptprb* deletion in mice or pharmacological VE-PTP inhibition in mice, rabbits and
339 humans lowers IOP (55-57), while rare *PTPRB* variants are associated with reduced glaucoma
340 risk (58). *Ptprb*/VE-PTP is highly expressed in blood vascular endothelial cells but is absent in
341 lymphatics (59), consistent with transcriptional suppression by PROX1.

342

343 *Schlemm's canal-specific Prox1 knockout mice as a model of ocular hypertension.*
344 Rodent genetic models of ocular hypertension have provided invaluable insights into glaucoma
345 pathogenesis, genetics and treatment. However, many existing models are developmental in
346 nature (60), exhibit very high IOP (60), are associated with ocular inflammation (61) or anterior
347 chamber abnormalities (62) that complicate interpretation. Other models, such as *MYOC* $^{Y437H}$
348 transgenic mice, have been reported to lose pressure elevation over time or exhibit environment-
349 specific effects, limiting their utility (63-65). Here, we report that Schlemm's canal specific
350 *Prox1* knockout mice developed significant IOP elevation as compared with contralateral control
351 eyes injected with control nanocarriers, and elevated IOP was maintained for at least 6 months.
352 In humans, ocular hypertension is defined as an IOP exceeding 21 mm Hg (66). As the
353 population-average IOP in humans is approximately 15 mm Hg (67), this corresponds to an
354 average pressure increase of more than 6 mmHg. In our study, baseline pressure was 10.7±0.4
355 mmHg (Figure 4B), and 8 weeks after induction had increased to 16.6±0.8 mmHg in *Prox1*
356 knockout eyes, a difference of 5.9 mmHg, slightly less than the pressure increase defined as

357 ocular hypertension in humans. Consistent with human ocular hypertension, no structural
358 abnormalities of the mouse aqueous outflow structures were observed. These findings suggest
359 our model may be valuable for future studies examining the impact of elevated IOP on retinal
360 function or testing IOP-lowering drugs.
361
362 *OHT nanocarriers are a valuable tool for targeted gene deletion.*
363 Combining the well-validated endothelial *Cdh5*-CreERT2 mouse strain with tissue specific
364 4OHT delivery via a targeted non-inflammatory nanocarrier (36, 68-70) allowed robust gene
365 deletion and increased tissue specificity without ocular toxicity. While adeno-associated viruses
366 (AAV) have been used in similar applications to generate models of eye disease (33) and for
367 gene therapy (71), ocular inflammation has been observed in patients (72-74) and rodent models
368 (75) following AAV administration. In contrast, the PEG-*b*-PPS platform is non-inflammatory
369 (76), can be customized for cell-specific targeting (36, 68-70) and can be adapted to deliver a
370 wide array of cargos and combinations thereof (36, 77, 78).

371 In addition to small diameter (~22 nm) that facilitated passage through the trabecular meshwork,
372 PEG-*b*-PPS nanocarriers are highly efficient at intracellular delivery (68, 79), improving
373 therapeutic effects at lower payload concentrations. This approach enhanced 4OHT efficacy for
374 driving recombination in nearly all targeted Schlemm's canal cells, while avoiding systemic
375 effects of pan-endothelial *Prox1* deletion. The 4OHT-loaded PEG-*b*-PPS nanocarriers are a
376 promising tool for achieving customizable and geographically targeted investigation of gene
377 expression in other tissues and models, with observed responses being attributed to specific gene
378 manipulation instead of non-specific inflammation or toxicity from tamoxifen or the delivery
379 vehicle itself.

380 *Limitations*

381 Our study has several limitations that deserve investigation beyond the scope of the present
382 manuscript. Prior reports (80) suggest the level of IOP elevation seen in Schlemm's canal
383 specific *Prox1* knockout eyes is likely to cause retinal ganglion cell loss and glaucoma. However,
384 this remains untested, and it is possible that low baseline IOP seen in *Prox1*$^{flox/flox}$;*Cdh5*-
385 CreERT2 mice prior to *Prox1* deletion will provide some protection from optic neuropathy. In
386 addition, while whole-mount immunostaining and penetrance of IOP elevation in nanocarrier-
387 induced *Prox1* knockout eyes indicated a consistent level of deletion, our Schlemm's canal-
388 specific approach combined with the presence of nearby PROX1-expressing lymphatic vessels
389 did not permit more sensitive whole-tissue quantification methods such as western blot or rtPCR.
390 Accordingly, we cannot exclude the possibility that increased deletion efficacy would further
391 elevate IOP—especially as the physical mechanism by which *PROX1* regulates aqueous humor
392 outflow resistance remains unknown. Our previous work (11, 12) highlighted the importance of
393 stiffness of the Schlemm's canal inner wall, and our finding of loss of the lymphatic phenotype in
394 our ocular hypertension mouse model is consistent with this model. Future studies examining
395 stiffness and gene expression in the canal endothelium after deletion or overexpression of
396 *PROX1* and related genes will help to elucidate the pathogenic mechanism.

397 Second, studies with *Flt4* knockout mice were performed using systemic administration of
398 tamoxifen rather than Schlemm's canal targeting nanocarriers, as unlike *Prox1* knockout mice,
399 these animals are viable if induced during adulthood. While we did not observe elevated IOP
400 following pan-endothelial *Flt4* deletion, *Flt4* is expressed by capillaries of the ciliary body (81)
401 in addition to Schlemm's canal and we cannot exclude the possibility that production of aqueous

402 humor was reduced in these animals. Future studies with canal-specific *Flt4* knockouts and
403 measurement of outflow facility are warranted.

404

405 *Conclusion*

406 Schlemm's canal-specific *Prox1* deletion in adult mice leads to long-lasting ocular hypertension
407 without canal degeneration or morphological changes. These findings demonstrate the
408 importance of the canal's lymphatic characteristics in the maintenance of normal aqueous humor
409 outflow resistance and highlight the phenotypic plasticity of Schlemm's canal as a target for
410 next-generation therapies for ocular hypertension. In addition to these mechanistic insights, our
411 studies also demonstrate the power of Schlemm's canal-specific 4OH-tamoxifen nanocarriers for
412 inducing robust, canal specific gene deletion without systemic phenotypes, as well as introduce
413 canal specific *Prox1* knockout mice as a new model of primary open-angle glaucoma.

414

415 **METHODS**

416 *Sex as a biological variable*

417 Animals of both sexes were included in all experiments at approximately equal ratios but were
418 analyzed together. Sex-specific analyses were not conducted.

419

420 *Study Approval*

421 Animal experiments were approved by the Animal Care and Use Committee at Northwestern
422 University (Evanston, IL) under animal protocol numbers IS00020857 and IS00022641 and

423 comply with the Association for Research in Vision and Ophthalmology guidelines for care and
424 use of vertebrate research subjects in ophthalmology research.

425

426 *Animal generation and husbandry*

427 Mice were housed at the Center for Comparative Medicine of Northwestern University (Chicago,
428 IL USA). Animals were provided with unlimited access to water and standard rodent diet (Teklad
429 #7912) and maintained on a standard 12-hour lighting cycle at a temperature of 21-23° and
430 relative humidity of 30-70%. To generate litters of *Rosa26*$^{mTmG}$; *Cdh5*-CreERT2 mice for
431 analysis, gt(ROSA)26Sortm4(ACTB-tdTomato,-EGFP)Luo/J (*Rosa26*$^{mTmG}$, Jax strain #007576)
432 (82) mice were crossed with Tg(Cdh5-cre/ERT2)$^{1Rha}$ animals carrying the *Cdh5*-CreERT2
433 transgene (83). *Prox1*$^{flox/flox}$ mice were a generous gift of Dr. Guillermo Oliver (Northwestern
434 University, Chicago, IL) (43, 45), and *Flt4*-floxed mice were a gift of Dr. Susan Quaggin
435 (Northwestern University, Chicago, IL) (84). Throughout the study, animals were maintained on
436 a mixed genetic background, and animals of both sexes were included in all experiments. Mice
437 were genotyped by PCR using previously published primers.

438

439 *Primary human Schlemm's canal cell culture*

440 Primary human Schlemm's canal cells were a generous gift of Dr. W. Daniel Stamer (Duke
441 University, Durham, NC). For siRNA experiments, normal Schlemm's canal cells from clones
442 SC-68 and SC-91 were seeded in 6 well plates before transfection in triplicate groups using a
443 previously validated *PROX1*-specific siRNA (Dharmacon, Lafayette, CO, USA. #016913-00-
444 0005) (43) or matching scrambled siRNA control (Dharmacon #016913-00-0005) in combination

445 with RNAimax reagent (Invitrogen, Thermo Fisher Scientific, 13778075) according to
446 manufacturer's instructions. 72 hours after treatment, total RNA was collected using TRIzol
447 reagent (ThermoFisher Scientific #15596026) and purified (RNEasy MinElute cleanup kit;
448 Quagen, Hilden Germany) before generation of cDNA for real-time PCR or RNA sequencing.

449

450 *HUVEC cell culture*

451 Human Umbilical Vein Endothelial Cells (HUVECs) from pooled donors were purchased from
452 Lonza (Walkersville, MD, USA). All primary cells used in these studies were used at passage 4.
453 HUVECs were cultured in endothelial cell growth basal medium-2, (EBM™-2, Lonza)
454 supplemented with FBS and EGM™-2 Endothelial Cell Growth Medium-2 BulletKit™ (Lonza)
455 optimized for HUVEC culture. All cells were cultured at 37°C, 5% $CO_2$ in T25 flasks.

456

457 *Analysis of human corneal rims.*

458 Surplus corneal rim tissue was obtained following corneal transplant surgery, fixed (4%
459 formaldehyde) and cryosectioned using standard techniques. Tissues recovered and preserved for
460 transplant within 15 hours of death were accepted for analysis; tissue with longer recovery times
461 showed no PROX1 expression (data not shown). No restrictions were placed on the duration of
462 storage in cornea culture media prior to transplant surgery. Cryosections were washed and
463 blocked (5% donkey serum, 2.5% BSA in TBS containing 0.5% Triton X100) prior to overnight
464 incubation with primary antibodies at 4°. Sections were then washed and incubated with
465 appropriate alexafluor-labeled secondary antibodies. To quantify PROX1 expression within
466 Schlemm's canal, sections were co-stained using antibodies against PROX1 and the endothelial

467 transcription factor ERG and QuPath software was used to quantify PROX1 fluorescence
468 intensity in ERG-positive Schlemm's canal nuclei and background intensity in non-endothelial
469 ERG-negative, DAPI-positive nuclei in other cells of the iridocorneal angle. Identically prepared
470 sections from human pterygium tissue were used as a positive control for LYVE1 staining. A
471 complete list of primary antibodies used is provided in Supplemental table S1.

472

473 *Real-time quantitative PCR*

474 Following RNA purification, cDNA was prepared using the iScript Kit (Bio-Rad Laboratories,
475 Hercules CA USA) according to the manufacturer's instructions. Real-time PCR was then
476 performed using a QuanStudio3 instrument (ThermoFisher Scientific) and Power SYBR green
477 master mix (ThermoFisher Scientific). The following primers were used: GAPDH-Fwd: 5'-
478 AAGGTCATCCCAGAGCTGAA-3', GAPDH-Rev: 5'- CTGCTTCACCACCTTCTTGA-3',
479 PROX1-Fwd: 5'-GAGCCTCCGTGGAACTCA-3', PROX1-Rev: 5'-
480 TGGGCACAGCTCAAGAATC-3', TEK-Fwd: 5'- CCCCTATGGGTGTTCCTGT-3', TEK-Rev:
481 5'- GCTTACAATCTGGCCCGTAA-3', CCL21-Fwd: CGCAGCTACCGGAAGCAG-3',
482 CCL21-Rev: 5'-CTGCCTGAGAGCGCTTGC-3'.

483

484 *Western blot*

485 Following siRNA transfection as described above, triplicate samples of primary human
486 Schlemm's canal cells (clone SC-68) were lysed using Laemmli sample buffer containing 100
487 mM DTT and separated using a 4-15% acrylamide minigel (TGX, Bio-Rad Laboratories,
488 Hercules, CA USA). Proteins were transferred onto a PVDF membrane (Bio-Rad), blocked (5%

489 bovine serum albumen in TBS pH 7.5 with 0.05% Tween 20, 1 h at room temperature) before
490 incubation overnight with appropriate primary antibodies. Membranes were then washed (TBS
491 containing 0.05% tween 20), incubated with appropriate HRP-conjugated secondary antibodies
492 and visualized using ECL reagent. Images were captured using an iBright CL1500 imaging
493 system (ThermoFisher Scientific) before densitometry was performed using ImageJ software. A
494 complete list of primary antibodies used is provided in Supplemental table S1.

495

496

497 *RNA sequencing*

498 Primary human Schlemm's canal cell clone SC-68 was used for RNA sequencing. Following
499 RNA purification as described above, total RNA isolated from triplicate samples of siControl and
500 si*PROX1*-treated cells were provided to the NUSeq core of Northwestern University Feinberg
501 School of Medicine for library preparation (TruSeq Kit; Illumina, San Diego, CA) and
502 sequencing on an Illumina HiSeq 4000 instrument. Reads were then aligned to the human
503 genome and differential expression analysis was performed using DeSeq2 (85). Differentially
504 expressed genes were then filtered using the Benjamini-Hochberg method using a false discovery
505 threshold of 0.05 and representative genes were selected for the heat map shown in Figure 1F.

506

507 *Solid-phase peptide synthesis*

508 Standard Fmoc solid-phase peptide synthesis was performed to synthetize the FLT4-binding
509 targeting peptide (Figure 2A). Fmoc-N-amido-dPEG$_{24}$ (Quanta Biodesign) were used in
510 synthesis of the PG48 peptide constructs.

511

512 *Nanocarrier generation and optimization*

513 All polymers used for nanocarrier formulation were synthesized based on previously established
514 procedures (35). Briefly, 40 mg of polymer, 136 µg 4OH-Tamoxifen (4OHT, H6278, Millipore
515 Sigma, St. Louis MO) and 5 µL of DiI dye (42364-100MG, Sigma-Aldrich)) were dissolved in
516 500 µL of tetrahydrofuran (THF). This mixture was then added dropwise to 1 mL of Phosphate
517 Buffer Saline (PBS, pH 7.5) under constant rotation. Nanocarrier solution was left in a desiccator
518 to remove THF overnight. FLT4 binding peptide (5% molar ratio) was dissolved in DMSO and
519 incorporated with targeted nanocarriers by gentle rotation. Blank nanocarriers were synthesized
520 by the same procedure without addition of 4OHT. Finally, the nanocarriers were purified and
521 concentrated to a final volume of 250 µL. Drug concentration and particle size were
522 characterized by High Performance Liquid Chromatography (HPLC) and Dynamic Light
523 Scattering (DLS).

524

525 *Quantification of 4OHT loading into nanocarriers*

526 50 mL aliquots of nanocarrier solution were frozen and freeze-dried. Resulting powder was
527 dissolved in methanol and precipitated at -20°C. Solution was then centrifuged (4000*g, 5 m) to
528 separate the precipitated polymer, and supernatant was collected and analyzed. 4OHT
529 concentration was determined using HPLC, with calibration against a 4OHT concentration series
530 (Supplemental Figure 3D and E) prepared in methanol. Absorbance was measured at 235 nm.
531 Data was obtained from three replicate samples, and HPLC was conducted using a C18 XDB-
532 Eclipse column (Agilent) with a static mobile phase of acetonitrile (ACN) and 0.1% TFA HPLC

533 water (85:15). 4OHT encapsulation efficiency (EE%) provided as a percentage was calculated as

534 $\frac{(M_i - M_u)}{M_i}$ x 100, where $M_i$ in the input mass of 4OHT and $M_u$ is the mass of unencapsulated 4OHT.

535

536 *Quantification of nanocarrier size, polydispersity, and zeta potential*

537 To determine particle diameter size and polydispersity index (PDI), 10 mL aliquots of targeted

538 and untargeted nanocarriers were diluted in PBS at a 10% v/v concentration and characterized by

539 DLS using a Zetasizer Nano instrument (Malvern Instruments) equipped with a 4 mW He-Ne

540 633 nm laser. Diameter of spherical nanocarriers and PDI were determined based on the intensity

541 average size distributions (n=3). Zeta ζ potential was measured using a Zetasizer Nano device

542 (Malvern Instruments). Average ζ potential for each nanocarrier was determined (n=3).

543

544 *Cryogenic Transmission Electron Microscopy*

545 Copper grids (200 mesh) with a lacey carbon membrane (Cat# LC200-Cu-100; Electron

546 Microscopy Sciences, Hatfield, PA) were glow-discharged in a Pelco easiGlow Discharge

547 Cleaning System. A sample volume (4 mL) was added to the grid and blotted for 5 seconds with

548 a blot offset of 0.5 mm and plunged into liquid ethane within a FEI Vitrobot Mark III plunge

549 freezing instrument. Samples were imaged using a JEOL JEM1230 Lab5 emission TEM (JEOL

550 USA) operating at 100 kEV.

551

552 *Small-Angle X-ray Scattering (SAXS)*

553 SAXS experiments were carried out at the 5-ID beamline of the DuPont–Northwestern–Dow

554 Collaborative Access Team (DND-CAT) located at the Advanced Photon Source at Argonne
555 National Laboratory. Measurements were obtained using collimated X-rays with a wavelength
556 (λ) of 1.24 Å (9 keV). Samples were prepared at a concentration of 5 mg/mL and loaded into an
557 in-vacuum flow cell using quartz capillaries with a thickness of 1.6 mm. Scattering data were
558 recorded over a q-range of 0.0015–0.08 $Å^{-1}$ with a sample-to-detector distance of approximately
559 8.5 m and an exposure time of 5 s. The momentum transfer, q, is defined as: $q=(4\pi/\lambda)\sin(\theta)$,
560 where 2θ represents the scattering angle. Data processing, including reduction and buffer
561 subtraction, was performed using BioXTAS RAW, while model fitting and analysis were
562 conducted with SasView.

563

564 *In vitro biocompatibility of 4OHT nanocarriers*

565 The 3-(4,5-Dimethylthiazol-2-yl)-2,5-Diphenyltetrazolium Bromide (MTT) assay was employed
566 to measure cell viability following incubation with nanocarriers. HUVECs, at a concentration of
567 $5x10^5$ cells/mL determined by cell counting, were seeded into U-bottom 96-well plates, with 200
568 µL of cell suspension per well. Each well received nanocarriers in 3 replicates, prepared in PBS
569 with a final 4OHT concentrations of 0, 0.5, 1, and 2 µM. Cells were incubated with nanocarriers
570 for 24 hours at 37 °C and 5% $CO_2$. MTT reagent, prepared at 5 mg/mL in PBS, was added to
571 each well (20 µL per well) and the cells were incubated for an additional 6 hours protected from
572 light. Afterward, the plates were centrifuged at 500 x g for 5 minutes, and the supernatant was
573 discarded. The formazan crystals formed in the wells were dissolved with 200 µL of dimethyl
574 sulfoxide (DMSO), and absorbance at 570 nm was measured using a SpectraMax M3 microplate
575 reader (Molecular Devices). Cell viability was then calculated as $\frac{OD_T}{OD_U}x100\%$ where $OD_T$

576 represents optical density of the nanocarrier treated sample and $OD_U$ corresponds to optical
577 density of the untreated sample (n=3).

578

579 *Nanocarrier uptake studies*

580 A total of 100,000 HUVECs or primary human Schlemm's canal cells were plated in each well
581 of 24-well polystyrene plates (Falcon) and allowed to adhere overnight at 37 °C with 5% $CO_2$.
582 The cells were exposed to nanocarriers for 2 hours, with all incubations conducted at 37 °C and
583 5% $CO_2$. Following the nanocarrier treatment, cells were harvested by mechanical scraping and
584 then stained with fixable Zombie Aqua viability dye (Biolegend, San Diego, CA) for 20 minutes
585 at 4 °C to evaluate cytotoxicity by flow cytometry. Flow cytometry was performed using a BD
586 LSRFortessa 6-Laser Flow Cytometer, recording 10,000 single-cell events per sample. Data were
587 analyzed using FlowJo software. Median fluorescence intensity (MFI) was normalized by
588 subtracting the average MFI from untreated cells and used to assess nanocarrier uptake.

589

590 *Intracameral injection of 4OHT nanocarriers in mice*

591 Mice were anesthetized with isoflurane and topical 0.5% proparacaine was provided for local
592 analgesia. A 35G beveled needle (World Precision Instruments, NF35BL) was inserted into the
593 anterior chamber and 3 μL nanocarrier solution was injected at a flow rate of 100 nL/min for 30
594 minutes using a micro digital syringe pump (UMP3, World Precision Instruments, Sarasota, FL).
595 Following injection, topical ophthalmic antibiotic (Neo-Poly-Bac, Bausch + Lomb, Chapel Hill,
596 NC) was applied to both eyes. Mice then received a single subcutaneous injection of Meloxicam

597 (20mg/kg B.W.) for analgesia. A second administration of topical antibiotic was provided 24
598 hours later.

599

600 *Tonometric IOP measurements*

601 Mice were anesthetized with ketamine/xylazine cocktail (ketamine 112.5 mg/kg, xylazine 2.5
602 mg/kg), and IOP measurements were taken 5–7 minutes post-anesthesia with a Tonolab rebound
603 tonometer (iCare, Vantaa Finland). Individual Tonolab measurements represent averages of six
604 individual recordings and IOP values reported in the manuscript are averaged from three
605 measurements.

606

607 *In vivo visible light OCT imaging and Schlemm's canal measurement*

608 Visible light OCT (vis-OCT) uses shorter wavelengths than commonly used OCTs, thereby
609 allowing for higher axial resolution and higher backscattering contrast in tissue. vis-OCT was
610 performed using a custom-built OCT system mounted on a robotic arm as previously described
611 to image the full 360° of the AHO pathway (86). The system operated over a 510–610 nm
612 spectral range, providing a theoretical axial resolution of 1.3 μm and a lateral resolution of 9.4
613 μm in tissue (86, 87). To achieve optimal sampling density while maintaining a compact imaging
614 field, the lateral field of view for each volumetric scan was configured to 1.58 mm × 1.58 mm.

615 *In vivo* imaging was performed on mice under general anesthesia using an intraperitoneal
616 injection (10 mL/kg body weight) of a ketamine/xylazine cocktail (11.45 mg/mL ketamine and
617 1.7 mg/mL xylazine in saline). To expose the limbal region for imaging, small relaxing incisions

618 were made at the nasal and temporal canthi and inserted a circular eyelid speculum beneath the
619 eyelids. During the imaging, a robotic arm (Meca500, Mecademic Inc.) precisely rotated the vis-
620 OCT imaging head around the optical axis of the eye, enabling acquisition of eight volumetric
621 vis-OCT datasets evenly distributed around the limbus at 45° intervals (87). Each volume
622 comprised 512 A-lines per B-scan and 512 B-scans per volume, collected using a temporal
623 speckle-averaging acquisition protocol in which each B-scan was repeated twice per volume to
624 improve signal-to-noise ratio and reduce speckle variation (88). The imaging beam was delivered
625 at an A-line rate of 75 kHz with an incident optical power of 1 mW at the cornea. All quadrants
626 of the mouse eye were imaged at the same height relative to the imaging beam to ensure uniform
627 sampling of the circumferential Schlemm's Canal structures.

628 For quantitative assessment of Schlemm's canal lumen dimensions, we analyzed two
629 representative B-scans per vis-OCT volume, resulting in 16 B-scans per eye across the whole
630 360° imaging sequence. Each selected B-scan was chosen based on optimal visualization of the
631 lumen and surrounding anatomical landmarks. The canal boundaries were manually segmented
632 using MATLAB's Volume Segmenter application, delineating the canal's area using the
633 paintbrush tool. The cross-sectional area of Schlemm's canal was calculated for each segmented
634 B-scan.

635

636 *Whole-mount imaging of mouse Schlemm's canal*.

637 Schlemm's canal imaging was performed as previously described (89). Briefly, whole globes
638 were enucleated, fixed (2% formaldehyde in PBS, pH 7.5), and dissected to remove the lens and
639 retina. Globes were then incubated overnight in lysis/blocking buffer (5% donkey serum, 3%

640 bovine serum albumen in TBS pH 7.5 containing 0.5% triton X 100) prior to an additional
641 overnight incubation in primary antibodies diluted in additional blocking buffer. Eyes were then
642 washed, incubated with alexafluor-conjugated secondary antibodies and mounted for imaging.
643 Images were captured using a Nikon A1R or Zeiss LSM 680 confocal microscope equipped with
644 a 20x objective. 10-15-image Z stacks were obtained, and maximum intensity projections
645 generated using Fiji software are shown in the manuscript. For quantification, 2-4 stacks were
646 collected at intervals around the circumference of the eye and total fluorescence projections
647 obtained using the "Sum Slices" function in ImageJ Fiji. Quantification of background
648 subtracted protein expression and canal area were obtained from these images and averaged to
649 obtain the values reported in the manuscript. A complete list of primary antibodies used is
650 provided in Supplemental table S1.

651

652 *Light and electron microscopy of mouse Schlemm's canal.*

653 Mice were anesthetized using ketamine/xylazine cocktail and blood was cleared via cardiac
654 perfusion at a flow rate of 15 ml/minute (PBS containing 1 mg/ml lidocaine and 10U/ml
655 heparin). Following clearing, 50 ml of modified Karnovsky's fixative (2% paraformaldehyde and
656 2.5% glutaraldehyde in 0.1M phosphate buffer, pH 7.4) was infused at the same flow rate. Upon
657 completion of cardiac perfusion, eyes were enucleated, a small incision made to allow fluid
658 transfer and submerged in additional fixative for 24 hours. Radial wedges containing trabecular
659 meshwork and Schlemm's canal were then collected from the nasal, inferior, superior and
660 temporal quadrants and prepared for ultramicrotomy and imaging as previously reported (90).
661 Briefly, wedges were post-fixed (1% $OsO_4$, 1% $La(NO_3)_3$, 2h) before staining with 1.5% uranyl
662 acetate. Tissues were then dehydrated, washed with propylene oxide and embedded in Epon-

663 Araldite using standard procedures. Gross canal morphology was analyzed in toluidine blue-
664 stained 4 µm semithin sections by a masked investigator using ImageJ. Reported values represent
665 averages of 7-8 sections per eye, with 1-2 sections collected from each quadrant. For electron
666 microscopy, ultrathin sections (70-80 nm) were prepared and imaging was performed using a
667 JEOL JEM-1400Flash transmission electron microscope equipped with a NanoSprint43 cMOS
668 camera.

669

670 *Statistical analysis and figure preparation*

671 Statistical analysis was performed using Prism 10.6 software (Graphpad Software LLC). Tests
672 used to obtain reported p values are described in figure legends. For all figures * indicates $p <$
673 $0.05$, ** $p < 0.01$, *** $p < 0.001$. Figures were prepared using Prism 10.6, Illustrator 29.8.1 and
674 InDesign 20.5 software (Adobe Inc, San Jose CA, USA). Image analysis and quantification was
675 performed using ImageJ Fiji (91). Except where noted, all error bars shown in figures indicate
676 SEM.

677

678 *Data availability*

679 Raw transcriptomics data is available in the Gene Expression Omnibus (GEO) using accession
680 number GSE310660. A table of all differentially expressed genes identified after si*PROX1*
681 treatment and used to generate figure 1F is provided as Supplemental data set 1. Raw data
682 underlying other figures are available from the authors upon reasonable request.

683

684 **FUNDING SUPPORT**

685 This work was supported by NIH R01 R01EY033813 (To MJ and EAS), a Northwestern
686 University Catalyst Grant (To MJ and BRT), and the Christina Enroth-Cugell Graduate Research
687 Award (To SLO). BRT also received support from NIH R01 R01EY032609 and Brightfocus
688 Foundation grant M2021018N. Imaging was performed at the Center for Advanced Microscopy
689 of the Feinberg School of Medicine, supported by NCI CCSG P30 CA060553 and at the Boston
690 University Transmission Electron Microscopy Core, supported by NIH grant S10 OD028571. We
691 also acknowledge support from George M. O'Brien kidney core grant P30 DK114857, and a
692 challenge grant from Research to Prevent Blindness to the Feinberg School of Medicine
693 Department of Ophthalmology.

694 **ACKNOWLEDGEMENTS**

695 Authors are grateful to Drs. Guillermo Oliver and Susan E. Quaggin (Northwestern University
696 Feinberg School of Medicine) for the generous gifts of *Prox1*-floxed and *Flt4*-floxed mice,
697 respectively, and for many valuable discussions. We are also indebted to Dr. W. Daniel Stamer
698 (Duke University School of Medicine) for the gift of primary human Schlemm's canal
699 endothelial cells. Technical support was provided by Sol Misener and Kyron McAllister.

700 **AUTHOR CONTRIBUTIONS**

701 BRT, MJ and EAS conceived of the study. SLO, BRT, MJ, EAS, HG, HFZ, ZY and HLL
702 designed experiments and analyzed results. SLO, MPV, HLL, NCM, PL, ZY, HJL and BRT
703 conducted experiments. SLO, BRT, MJ and EAS wrote the manuscript. All authors contributed to
704 editing the manuscript and validation of results.

705 **REFERENCES**


706 1. Quigley HA, and Broman AT. The number of people with glaucoma worldwide in 2010
707 and 2020. *Br J Ophthalmol.* 2006;90(3):262-7. DOI: 10.1136/bjo.2005.081224

708 2. Kass MA, et al. The ocular hypertension treatment study: A randomized trial determines
709 that topical ocular hypotensive medication delays or prevents the onset of primary open-
710 angle glaucoma. *Arch Ophthalmol.* 2002;120(6):701-13. DOI:
711 10.1001/archopht.120.6.701

712 3. De Moraes CG, et al. Effect of treatment on the rate of visual field change in the ocular
713 hypertension treatment study observation group. *Invest Ophthalmol Vis Sci.*
714 2012;53(4):1704-9. DOI: 10.1167/iovs.11-8186

715 4. Ederer F, et al. The advanced glaucoma intervention study (agis): 1. Study design and
716 methods and baseline characteristics of study patients. *Control Clin Trials.*
717 1994;15(4):299-325. DOI: 10.1016/0197-2456(94)90046-9

718 5. Sheybani A, et al. Open-angle glaucoma: Burden of illness, current therapies, and the
719 management of nocturnal iop variation. *Ophthalmol Ther.* 2020;9(1):1-14. DOI:
720 10.1007/s40123-019-00222-z

721 6. Grant WM. Clinical measurements of aqueous outflow. *Am J Ophthalmol.*
722 1951;34(11):1603-5. DOI:

723 7. Leber T. Studien über den flüssigkeitswechsel im auge. *Albrecht von Graefes Archiv für*
724 *Ophthalmologie.* 1873;19(2):87-185. DOI: 10.1007/BF01720618

725 8. Johnson M, et al. Modulation of outflow resistance by the pores of the inner wall
726 endothelium. *Invest Ophthalmol Vis Sci.* 1992;33(5):1670-5. DOI:

727 9. Allingham RR, et al. The relationship between pore density and outflow facility in human
728 eyes. *Invest Ophthalmol Vis Sci.* 1992;33(5):1661-9. DOI:

729 10. Johnson M, et al. The pore density in the inner wall endothelium of schlemm's canal of
730 glaucomatous eyes. *Invest Ophthalmol Vis Sci.* 2002;43(9):2950-5. DOI:

731 11. Overby DR, et al. Altered mechanobiology of schlemm's canal endothelial cells in
732 glaucoma. *Proc Natl Acad Sci U S A.* 2014;111(38):13876-81. DOI:
733 10.1073/pnas.1410602111

734 12. Vahabikashi A, et al. Increased stiffness and flow resistance of the inner wall of
735 schlemm's canal in glaucomatous human eyes. *Proceedings of the National Academy of*
736 *Sciences.* 2019;116(52):26555-63. DOI: doi:10.1073/pnas.1911837116

737 13. Zhou EH, et al. Mechanical responsiveness of the endothelial cell of schlemm's canal:
738 Scope, variability and its potential role in controlling aqueous humour outflow. *J R Soc*
739 *Interface.* 2012;9(71):1144-55. DOI: 10.1098/rsif.2011.0733

740 14. Raviola G, and Raviola E. Paracellular route of aqueous outflow in the trabecular
741 meshwork and canal of schlemm. A freeze-fracture study of the endothelial junctions in
742 the sclerocorneal angel of the macaque monkey eye. *Invest Ophthalmol Vis Sci.*
743 1981;21(1 Pt 1):52-72. DOI:

744 15. Ramos RF, et al. Schlemm's canal endothelia, lymphatic, or blood vasculature? *J*
745 *Glaucoma.* 2007;16(4):391-405. DOI: 10.1097/IJG.0b013e3180654ac6

16. Pawlak JB, and Caron KM. Lymphatic programing and specialization in hybrid vessels. *Front Physiol.* 2020;11(114-. DOI: 10.3389/fphys.2020.00114

17. Kenig-Kozlovsky Y, et al. Ascending vasa recta are angiopoietin/tie2-dependent lymphatic-like vessels. *Journal of the American Society of Nephrology.* 2017. DOI: 10.1681/asn.2017090962

18. Hong SP, et al. Three-dimensional morphologic and molecular atlases of nasal vasculature. *Nature Cardiovascular Research.* 2023;2(5):449-66. DOI: 10.1038/s44161-023-00257-3

19. Pawlak JB, et al. Lymphatic mimicry in maternal endothelial cells promotes placental spiral artery remodeling. *The Journal of clinical investigation.* 2019;129(11):4912-21. DOI:

20. Schnabellehner S, et al. Penile cavernous sinusoids are prox1-positive hybrid vessels. *Vascular Biology.* 2024;6(1):e230014. DOI: 10.1530/VB-23-0014

21. Kizhatil K, et al. Schlemm's canal is a unique vessel with a combination of blood vascular and lymphatic phenotypes that forms by a novel developmental process. *PLoS Biol.* 2014;12(7):e1001912. DOI: 10.1371/journal.pbio.1001912

22. O'morchoe CC, and O'morchoe PJ. Differences in lymphatic and blood capillary permeability: Ultrastructural-functional correlations. *Lymphology.* 1987;20(4):205-9. DOI:

23. Oliver G. Lymphatic endothelial cell fate specification in the mammalian embryo: An historical perspective. *Dev Biol.* 2022;482(44-54. DOI: 10.1016/j.ydbio.2021.12.005

24. Johnson M. What controls aqueous humour outflow resistance? *Exp Eye Res.* 2006;82(4):545-57. DOI: 10.1016/j.exer.2005.10.011

25. Aspelund A, et al. The schlemm's canal is a vegf-c/vegfr-3–responsive lymphatic-like vessel. *The Journal of Clinical Investigation.* 2014;124(9):3975-86. DOI: 10.1172/JCI75395

26. Van Der Merwe EL, and Kidson SH. The three-dimensional organisation of the post-trabecular aqueous outflow pathway and limbal vasculature in the mouse. *Exp Eye Res.* 2014;125(0):226-35. DOI: 10.1016/j.exer.2014.06.011

27. Thomson B, et al. Cellular crosstalk regulates the aqueous humor outflow pathway and provides new targets for glaucoma therapies. *GitHub.* 2021. DOI: 10.5281/zenodo.5172757

28. Kim J, et al. Impaired angiopoietin/tie2 signaling compromises schlemm's canal integrity and induces glaucoma. *The Journal of Clinical Investigation.* 2017;127(10):3877-96. DOI: 10.1172/JCI94668

29. Park D-Y, et al. Lymphatic regulator prox1 determines schlemm's canal integrity and identity. *The Journal of Clinical Investigation.* 2014;124(9):3960-74. DOI: 10.1172/JCI75392

30. Reina-Torres E, et al. Vegf as a paracrine regulator of conventional outflow facility. *Invest Ophthalmol Vis Sci.* 2017;58(3):1899-908. DOI: 10.1167/iovs.16-20779

31. Thomson BR, et al. Angiopoietin-1 knockout mice as a genetic model of open-angle glaucoma. *Translational Vision Science & Technology.* 2020;9(4):16-. DOI: 10.1167/tvst.9.4.16

789 32. Thackaberry EA, et al. Rapid development of glaucoma via itv nonselective angpt 1/2
790 antibody: A potential role for angpt/tie2 signaling in primate aqueous humor outflow.
791 *Invest Ophthalmol Vis Sci.* 2019;60(13):4097-108. DOI: 10.1167/iovs.18-26349
792 33. Schwakopf J, et al. Schlemm's canal-selective tie2/tek knockdown induces sustained
793 ocular hypertension in adult mice. *Exp Eye Res.* 2024;248(110114. DOI:
794 10.1016/j.exer.2024.110114
795 34. Stack T, et al. Modulation of schlemm's canal endothelial cell stiffness via latrunculin
796 loaded block copolymer micelles. *J Biomed Mater Res A.* 2018;106(7):1771-9. DOI:
797 10.1002/jbm.a.36376
798 35. Stack T, et al. Targeted delivery of cell softening micelles to schlemm's canal endothelial
799 cells for treatment of glaucoma. *Small.* 2020;16(43):2004205. DOI:
800 https://doi.org/10.1002/smll.202004205
801 36. Vincent MP, et al. Surface engineering of flt4-targeted nanocarriers enhances cell-
802 softening glaucoma therapy. *ACS Applied Materials & Interfaces.* 2021;13(28):32823-36.
803 DOI: 10.1021/acsami.1c09294
804 37. Rashbrook VS, et al. Cre toxicity in mouse models of cardiovascular physiology and
805 disease. *Nat Cardiovasc Res.* 2022;1(806-16. DOI: 10.1038/s44161-022-00125-6
806 38. Van Zyl T, et al. Cell atlas of aqueous humor outflow pathways in eyes of humans and
807 four model species provides insight into glaucoma pathogenesis. *Proceedings of the*
808 *National Academy of Sciences.* 2020;117(19):10339. DOI: 10.1073/pnas.2001250117
809 39. Balasubramanian R, et al. Transcriptomic profiling of schlemm's canal cells reveals a
810 lymphatic-biased identity and three major cell states. *eLife.* 2024;13(RP96459. DOI:
811 10.7554/eLife.96459
812 40. Van Zyl T, et al. Cell atlas of the human ocular anterior segment: Tissue-specific and
813 shared cell types. *Proceedings of the National Academy of Sciences.*
814 2022;119(29):e2200914119. DOI: 10.1073/pnas.2200914119
815 41. Patel G, et al. Molecular taxonomy of human ocular outflow tissues defined by single-
816 cell transcriptomics. *Proceedings of the National Academy of Sciences.*
817 2020;117(23):12856. DOI: 10.1073/pnas.2001896117
818 42. Birke K, et al. Expression of podoplanin and other lymphatic markers in the human
819 anterior eye segment. *Invest Ophthalmol Vis Sci.* 2010;51(1):344-54. DOI:
820 10.1167/iovs.08-3307
821 43. Johnson NC, et al. Lymphatic endothelial cell identity is reversible and its maintenance
822 requires prox1 activity. *Genes Dev.* 2008;22(23):3282-91. DOI: 10.1101/gad.1727208
823 44. Srinivasan RS, et al. The prox1–vegfr3 feedback loop maintains the identity and the
824 number of lymphatic endothelial cell progenitors. *Genes Dev.* 2014;28(19):2175-87. DOI:
825 10.1101/gad.216226.113
826 45. Harvey NL, et al. Lymphatic vascular defects promoted by prox1 haploinsufficiency
827 cause adult-onset obesity. *Nat Genet.* 2005;37(10):1072-81. DOI: 10.1038/ng1642
828 46. Niec RE, et al. Lymphatics act as a signaling hub to regulate intestinal stem cell activity.
829 *Cell Stem Cell.* 2022;29(7):1067-82.e18. DOI: 10.1016/j.stem.2022.05.007

47. Gaasterland D, et al. Studies of aqueous humour dynamics in man. Vi. Effect of age upon parameters of intraocular pressure in normal human eyes. *Exp Eye Res.* 1978;26(6):651-6. DOI: 10.1016/0014-4835(78)90099-4

48. Brauch H, et al. Pharmacogenomics of tamoxifen therapy. *Clin Chem.* 2009;55(10):1770-82. DOI: 10.1373/clinchem.2008.121756

49. Ma W, et al. Mitochondrial respiration controls the prox1-vegfr3 feedback loop during lymphatic endothelial cell fate specification and maintenance. *Science Advances.* 2021;7(18):eabe7359. DOI: 10.1126/sciadv.abe7359

50. Wigle JT, and Oliver G. Prox1 function is required for the development of the murine lymphatic system. *Cell.* 1999;98(6):769-78. DOI: 10.1016/S0092-8674(00)81511-1

51. Petrova TV, et al. Lymphatic endothelial reprogramming of vascular endothelial cells by the prox-1 homeobox transcription factor. *The EMBO Journal.* 2002;21(17):4593-9-9. DOI: 10.1093/emboj/cdf470

52. Overby DR, et al. Ultrastructural changes associated with dexamethasone-induced ocular hypertension in mice. *Invest Ophthalmol Vis Sci.* 2014;55(8):4922-33. DOI: 10.1167/iovs.14-14429

53. Last JA, et al. Elastic modulus determination of normal and glaucomatous human trabecular meshwork. *Invest Ophthalmol Vis Sci.* 2011;52(5):2147-52. DOI: 10.1167/iovs.10-6342

54. Zhang RZ, et al. Length-tension relationships of small arteries, veins, and lymphatics from the rat mesenteric microcirculation. *Am J Physiol Heart Circ Physiol.* 2007;292(4):H1943-52. DOI: 10.1152/ajpheart.01000.2005

55. Thomson BR, et al. Targeting the vascular-specific phosphatase ptprb protects against retinal ganglion cell loss in a pre-clinical model of glaucoma. *eLife.* 2019;8(e48474. DOI: 10.7554/eLife.48474

56. Mishra S, et al. Inhibition of ve-ptp rejuvenates schlemm's canal in aged mice and acts via tie2. *PLoS One.* 2025;20(5):e0323615. DOI: 10.1371/journal.pone.0323615

57. Li G, et al. A small molecule inhibitor of ve-ptp activates tie2 in schlemm's canal increasing outflow facility and reducing intraocular pressure. *Invest Ophthalmol Vis Sci.* 2020;61(14):12-. DOI: 10.1167/iovs.61.14.12

58. Rämö JT, et al. Rare genetic variation in ptprb is associated with central serous chorioretinopathy, varicose veins and glaucoma. *Nat Commun.* 2025;16(1):4127. DOI: 10.1038/s41467-025-58686-6

59. Souma T, et al. Context-dependent functions of angiopoietin 2 are determined by the endothelial phosphatase veptp. *Proceedings of the National Academy of Sciences.* 2018. DOI: 10.1073/pnas.1714446115

60. Thomson BR, et al. A lymphatic defect causes ocular hypertension and glaucoma in mice. *The Journal of Clinical Investigation.* 2014;124(10). DOI: 10.1172/JCI77162

61. Biswas S, and Wan KH. Review of rodent hypertensive glaucoma models. *Acta Ophthalmol (Copenh).* 2019;97(3):e331-e40. DOI: 10.1111/aos.13983

62. Turner AJ, et al. Dba/2j mouse model for experimental glaucoma: Pitfalls and problems. *Clin Experiment Ophthalmol.* 2017;45(9):911-22. DOI: 10.1111/ceo.12992

872 63. Zhang X, et al. Intraocular pressure across the lifespan of tg-myocy437h mice. *Exp Eye*
873 *Res.* 2024;241(109855. DOI: 10.1016/j.exer.2024.109855
874 64. Bahranifard MR, et al. Magnetically steered cell therapy for reduction of intraocular
875 pressure as a treatment strategy for open-angle glaucoma. *eLife.* 2025;13(RP103256.
876 DOI: 10.7554/eLife.103256
877 65. Tolman NG, et al. Absence of glaucoma in tg-myocy437h mice of diverse genetic
878 backgrounds. *Invest Ophthalmol Vis Sci.* 2025;66(12):40. DOI: 10.1167/iovs.66.12.40
879 66. Jonas JB, et al. Ocular hypertension: General characteristics and estimated cerebrospinal
880 fluid pressure. The beijing eye study 2011. *PLoS One.* 2014;9(7):e100533. DOI:
881 10.1371/journal.pone.0100533
882 67. Wang YX, et al. Intraocular pressure and its normal range adjusted for ocular and
883 systemic parameters. The beijing eye study 2011. *PLoS One.* 2018;13(5):e0196926. DOI:
884 10.1371/journal.pone.0196926
885 68. Yi S, et al. Tailoring nanostructure morphology for enhanced targeting of dendritic cells
886 in atherosclerosis. *ACS Nano.* 2016;10(12):11290-303. DOI: 10.1021/acsnano.6b06451
887 69. Vincent MP, et al. Surface chemistry-mediated modulation of adsorbed albumin folding
888 state specifies nanocarrier clearance by distinct macrophage subsets. *Nat Commun.*
889 2021;12(1):648. DOI: 10.1038/s41467-020-20886-7
890 70. Vincent MP, et al. The combination of morphology and surface chemistry defines the
891 immunological identity of nanocarriers in human blood. *Adv Ther (Weinh).* 2021;4(4).
892 DOI: 10.1002/adtp.202100062
893 71. Russell S, et al. Efficacy and safety of voretigene neparvovec (aav2-hrpe65v2) in patients
894 with rpe65-mediated inherited retinal dystrophy: A randomised, controlled, open-label,
895 phase 3 trial. *Lancet.* 2017;390(10097):849-60. DOI: 10.1016/s0140-6736(17)31868-8
896 72. Cukras C, et al. Retinal aav8-rs1 gene therapy for x-linked retinoschisis: Initial findings
897 from a phase i/iia trial by intravitreal delivery. *Mol Ther.* 2018;26(9):2282-94. DOI:
898 10.1016/j.ymthe.2018.05.025
899 73. Lopez J, et al. Subretinal deposits in young patients treated with voretigene neparvovec-
900 rzyl for rpe65-mediated retinal dystrophy. *Br J Ophthalmol.* 2023;107(3):299-301. DOI:
901 10.1136/bjo-2022-321488
902 74. Gange WS, et al. Perifoveal chorioretinal atrophy after subretinal voretigene neparvovec-
903 rzyl for rpe65-mediated leber congenital amaurosis. *Ophthalmol Retina.* 2022;6(1):58-64.
904 DOI: 10.1016/j.oret.2021.03.016
905 75. Wiley LA, et al. The degree of adeno-associated virus-induced retinal inflammation
906 varies based on serotype and route of delivery: Intravitreal, subretinal, or suprachoroidal.
907 *Hum Gene Ther.* 2023;34(11-12):530-9. DOI: 10.1089/hum.2022.222
908 76. Kim H, et al. Filomicelle-embedded composite hydrogels for localized gelation within
909 the anterior chamber of the eye. *bioRxiv.* 2025:2025.08.19.671150. DOI:
910 10.1101/2025.08.19.671150
911 77. Yi S, et al. Surface engineered polymersomes for enhanced modulation of dendritic cells
912 during cardiovascular immunotherapy. *Advanced Functional Materials.*
913 2019;29(42):1904399. DOI: 10.1002/adfm.201904399

78. Burke JA, et Aal. Subcutaneous nanotherapy repurposes the immunosuppressive mechanism of rapamycin to enhance allogeneic islet graft viability. *Nature Nanotechnology.* 2022;17(3):319-30. DOI: 10.1038/s41565-021-01048-2

79. Vasdekis AE, et al. Precision intracellular delivery based on optofluidic polymersome rupture. *ACS Nano.* 2012;6(9):7850-7. DOI: 10.1021/nn302122h

80. Kaipa BR, et al. Impaired axonal transport contributes to neurodegeneration in a cre-inducible mouse model of myocilin-associated glaucoma. *JCI Insight.* 2025;10(5). DOI: 10.1172/jci.insight.188710

81. Kaser-Eichberger A, et al. Topography of lymphatic markers in human iris and ciliary body. *Invest Ophthalmol Vis Sci.* 2015;56(8):4943-53. DOI: 10.1167/iovs.15-16573

82. Muzumdar MD, et al. A global double-fluorescent cre reporter mouse. *Genesis.* 2007;45(9):593-605. DOI: 10.1002/dvg.20335

83. Sörensen I, et al. Dll1-mediated notch activation regulates endothelial identity in mouse fetal arteries. *Blood.* 2009;113(22):5680-8. DOI: 10.1182/blood-2008-08-174508

84. Donnan MD, et al. Formation of the glomerular microvasculature is regulated by vegfr-3. *American Journal of Physiology-Renal Physiology.* 2023;324(1):F91-F105. DOI: 10.1152/ajprenal.00066.2022

85. Love MI, et al. Moderated estimation of fold change and dispersion for rna-seq data with deseq2. *Genome Biol.* 2014;15(12):550. DOI: 10.1186/s13059-014-0550-8

86. Zhang X, et al. In vivo imaging of schlemm's canal and limbal vascular network in mouse using visible-light oct. *Invest Ophthalmol Vis Sci.* 2020;61(2):23-. DOI: 10.1167/iovs.61.2.23

87. Fang R, et al. Robotic optical coherence tomography with expanded three-dimensional field-of-view using point-cloud-based volumetric montaging. *IEEE Trans Med Imaging.* 2025;44(11):4639-51. DOI: 10.1109/tmi.2025.3580383

88. Zhang P, et al. Temporal speckle-averaging of optical coherence tomography volumes for in-vivo cellular resolution neuronal and vascular retinal imaging. *Neurophotonics.* 2019;6(4):041105. DOI: 10.1117/1.NPh.6.4.041105

89. Thomson BR, and Quaggin SE. In: Oliver G, and Kahn ML eds. *Lymphangiogenesis: Methods and protocols*. New York, NY: Springer New York; 2018:153-60.

90. Li HL, et al. Endothelial glycocalyx in different flow regions of the trabecular outflow pathway in bovine eyes. *Front Cell Dev Biol.* 2025;13(1569569. DOI: 10.3389/fcell.2025.1569569

91. Schindelin J, et al. Fiji: An open-source platform for biological-image analysis. *Nat Meth.* 2012;9(7):676-82. DOI: 10.1038/nmeth.2019

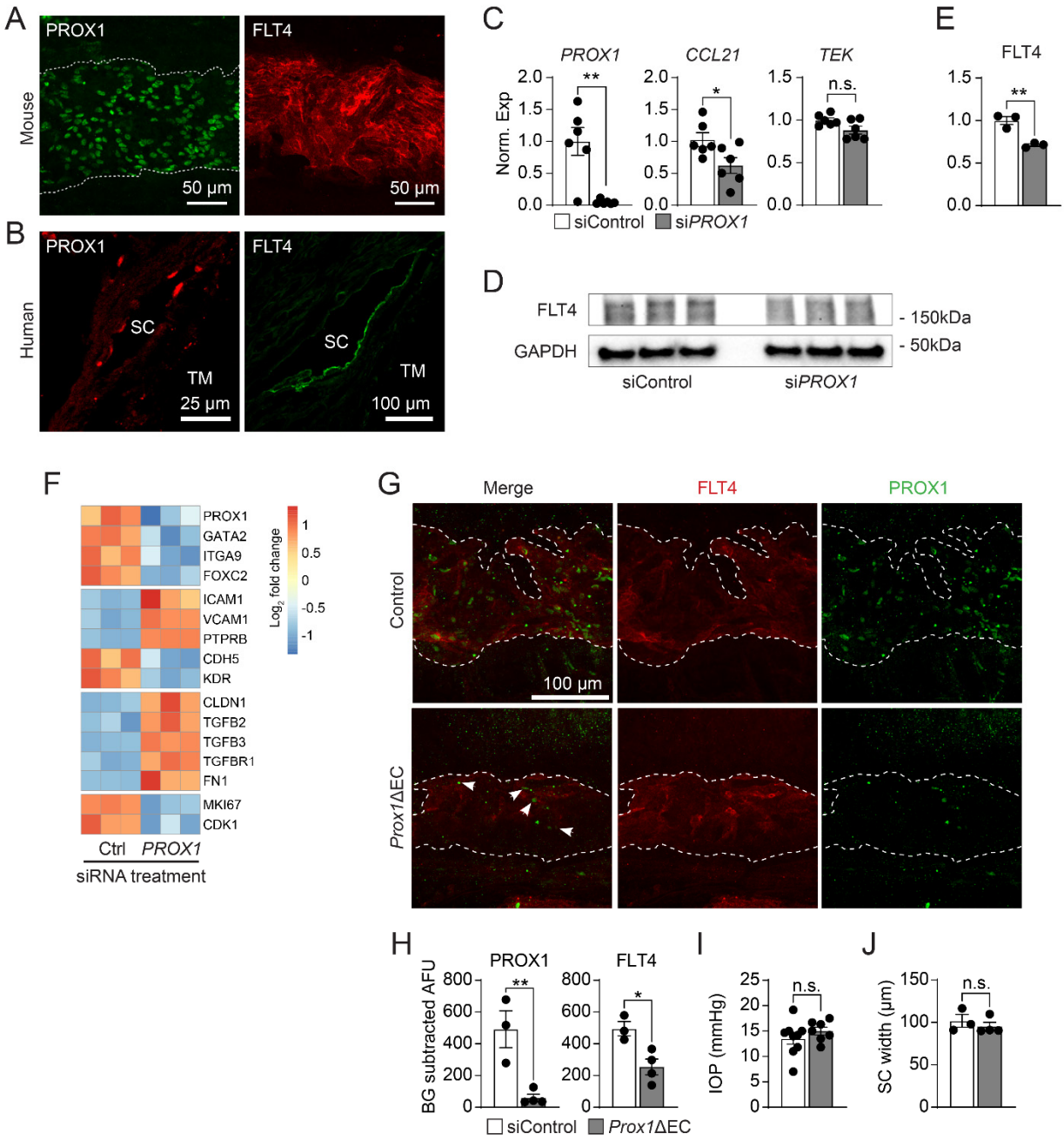
A
PROX1
FLT4
Mouse
50 μm
50 μm
B
PROX1
FLT4
Human
SC
TM
25 μm
SC
TM
100 μm
C
PROX1
CCL21
TEK
Norm. Exp
siControl
siPROX1
E
FLT4
D
FLT4
GAPDH
- 150kDa
- 50kDa
siControl
siPROX1
F
PROX1
GATA2
ITGA9
FOXC2
ICAM1
VCAM1
PTPRB
CDH5
KDR
CLDN1
TGFB2
TGFB3
TGFBR1
FN1
MKI67
CDK1
Log2 fold change
Ctrl
PROX1
siRNA treatment
G
Merge
FLT4
PROX1
Control
Prox1ΔEC
100 μm
H
PROX1
FLT4
BG subtracted AFU
siControl
Prox1ΔEC
I
IOP (mmHg)
n.s.
J
SC width (μm)
n.s.

950

951

952 **Figure 1. Human and mouse SC endothelial cells share a lymphatic-like hybrid phenotype**
953 **mediated by PROX1.** Whole mount immunostaining of mouse (**A**) and cryosections of human
954 (**B**) Schlemm's canals revealed robust expression of the lymphatic markers PROX1 and FLT4.
955 (**C**) *PROX1* and *CCL21* expression were reduced in primary human Schlemm's canal endothelial
956 cells treated with PROX1 siRNA, while levels of the universally expressed endothelial gene *TEK*
957 were unchanged when measured by real-time rtPCR (siControl n = 6, si*PROX1* n = 6). (**D**,
958 quantified in **E**) Western blot revealed reduced expression of FLT4 protein in siPROX1-treated
959 human Schlemm's canal cells (n = 3 per group). (**F**) Reduced expression of lymphatic genes and
960 increased expression of blood endothelial genes were detected in si*PROX1*-treated SC cells by
961 RNA sequencing, accompanied by increased expression of TGFB-signaling genes and reduction
962 in cell proliferation markers (n = 3 per group). (**G**, quantified in **H**) Confocal microscopy
963 Schlemm's canal flat mounts revealed reduced PROX1 and FLT4 expression in *Prox1*$^{flox/flox}$;
964 *Cdh5*-CreERT2 mice 4 weeks after tamoxifen induction at 8 weeks of age (*Prox1*ΔEC). While
965 *Prox1* deletion was generally robust, some mosaicism was observed, and a small number of
966 PROX1-positive nuclei were observed in *Prox1*ΔEC Schlemm's canal (white arrowheads,
967 *Prox1*ΔEC n = 3, Control n = 4). Dashed lines in **G** outline Schlemm's canal. (**I**) No significant
968 change in IOP (*Prox1*ΔEC n = 9, Control n = 7) or (**J**) Schlemm's canal width (*Prox1*ΔEC n = 3,
969 Control n = 4) was measured 4 weeks after whole-body tamoxifen induction. * $p < 0.05$, ** $p$
970 $< 0.01$ as determined by 2-tailed, unpaired Student's t test. Error bars in **C**, **E**, **H** and **I** indicate
971 ±SEM, while each point denotes an independent biological replicate.

972

973

974

975

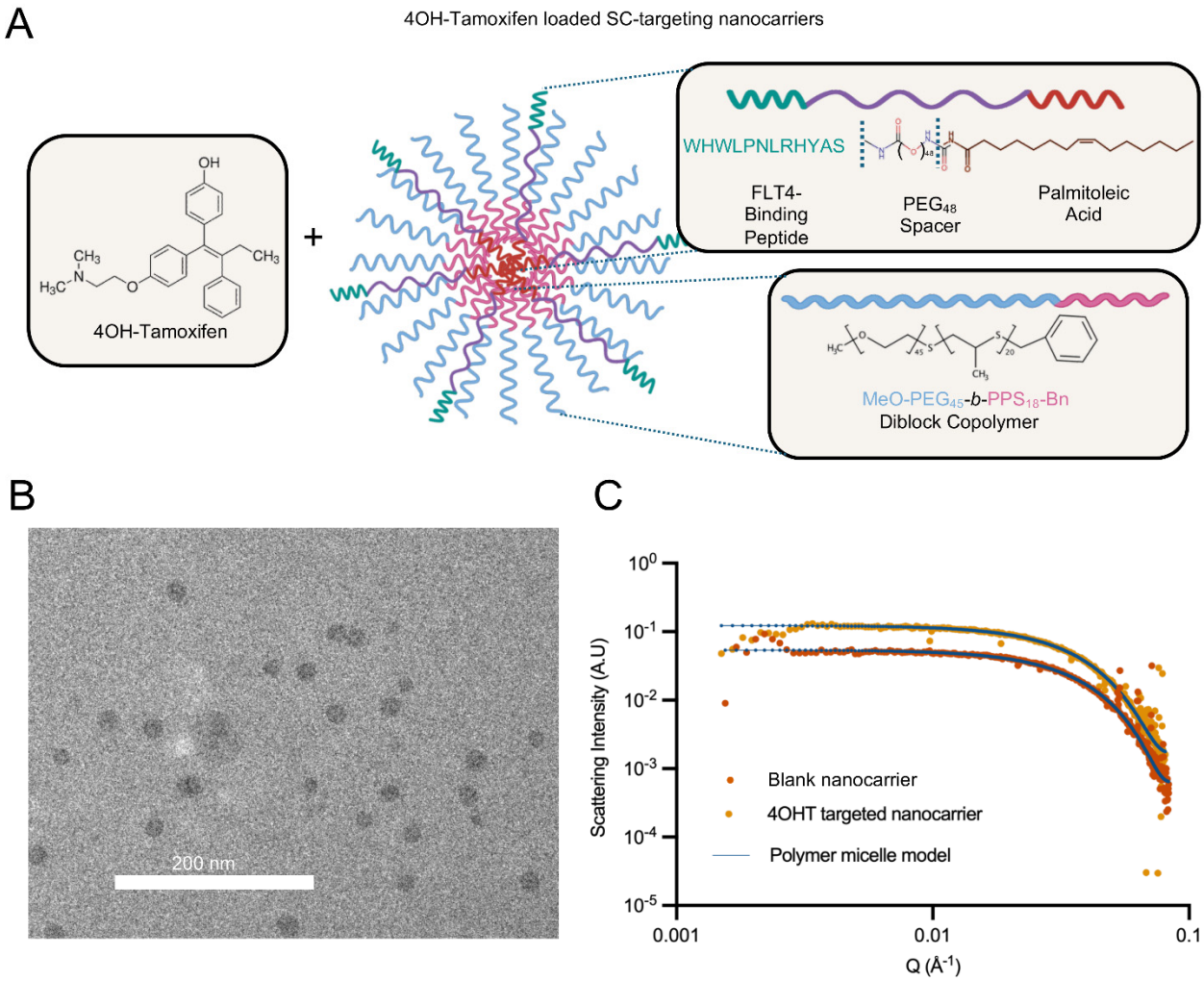


**Figure 2. Characterization of targeted and untargeted 4OH-Tamoxifen (4OHT) loaded nanocarriers (Targeted 4OHT/Untargeted 4OHT)** (**A**) Schematic illustrating how PEG-*b*-PPS targeted nanocarriers are generated and loaded with 4OHT. (**B**) Micellar morphology for 4OHT nanocarriers was characterized by **(B)** cryogenic transmission electron microscopy (Cryo-TEM) and (**C**) small angle X-ray scattering (SAXS, n= 2). The targeted PEG-*b*-PPS nanocarrier platform was previously validated and optimized for selective drug delivery to SC cells *in vitro* and *in vivo* (36).

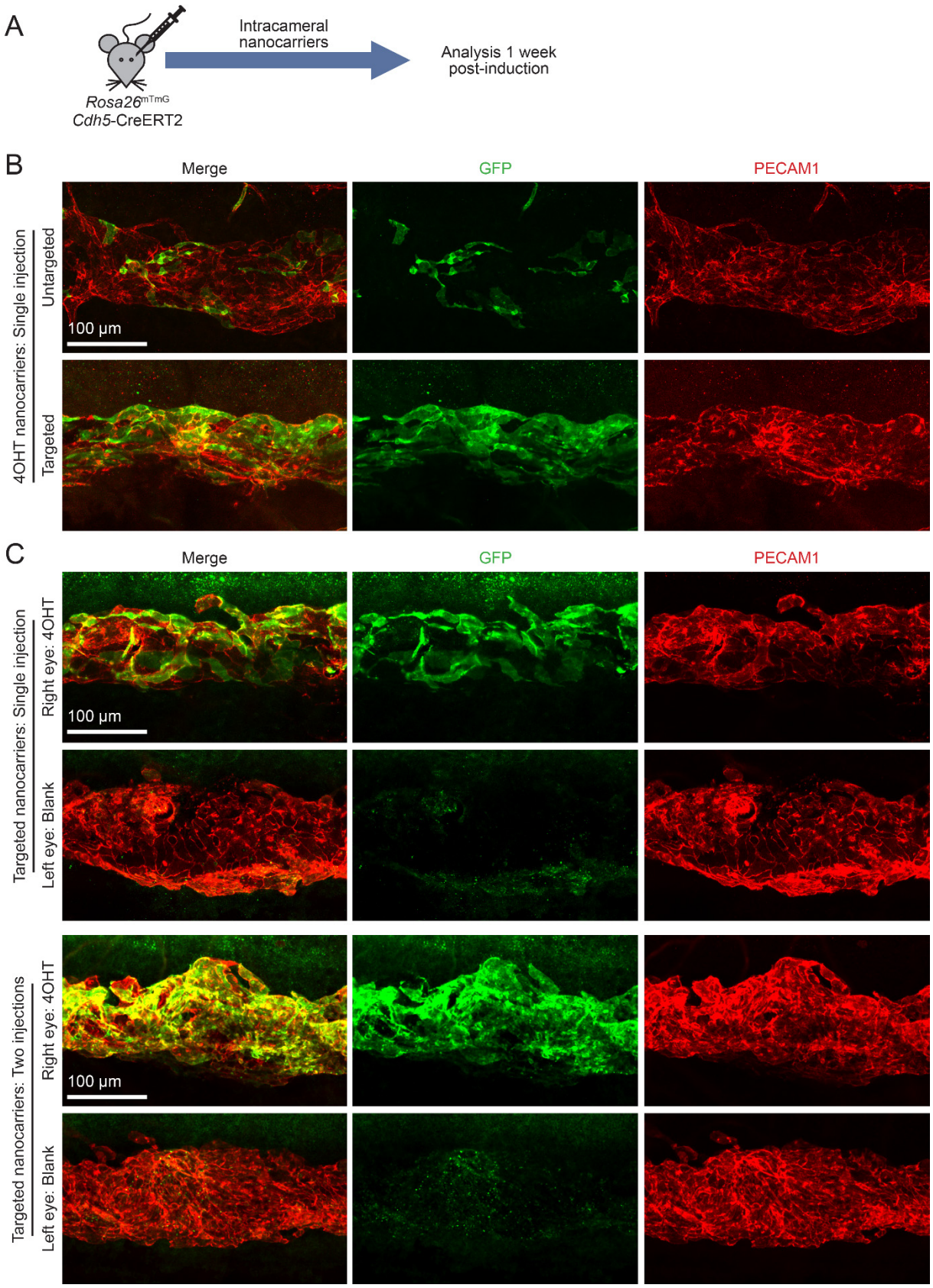
A
Intracameral nanocarriers
Analysis 1 week post-induction
Rosa26mTmG
Cdh5-CreERT2
B
Merge
GFP
PECAM1
4OHT nanocarriers: Single injection
Untargeted
Targeted
100 µm
C
Merge
GFP
PECAM1
Targeted nanocarriers: Single injection
Right eye: 4OHT
Left eye: Blank
100 µm
Targeted nanocarriers: Two injections
Right eye: 4OHT
Left eye: Blank
100 µm

986

987 **Figure 3. 4OH tamoxifen loaded, Schlemm's canal (SC) targeted nanocarriers induce**
988 **robust cre-mediated recombination.** (**A**) Schematic of experimental timeline used for
989 nanocarrier induction. (**B**) Seven days after intracameral infusion of untargeted 4OHT-loaded
990 nanocarriers, only sporadic recombination of SC endothelial cells was observed in *Rosa26*$^{mTmG}$;
991 *Cdh5*-CreERT2 mice (GFP expression). In contrast, robust recombination was induced by
992 nanocarriers labeled with FLT4 targeting peptide, indicating enhanced uptake by the SC
993 endothelium. (**C**) SC-specific recombination efficiency was further increased by a second
994 injection of FLT4-targeting nanocarriers 24h after the first. No recombination was observed in
995 SC of contralateral eyes that received infusions of identical targeted nanocarriers lacking 4OHT
996 cargo (blank nanocarriers) as a negative control, confirming specificity of the system and lack of
997 systemic recombination following nanocarrier treatment.

998

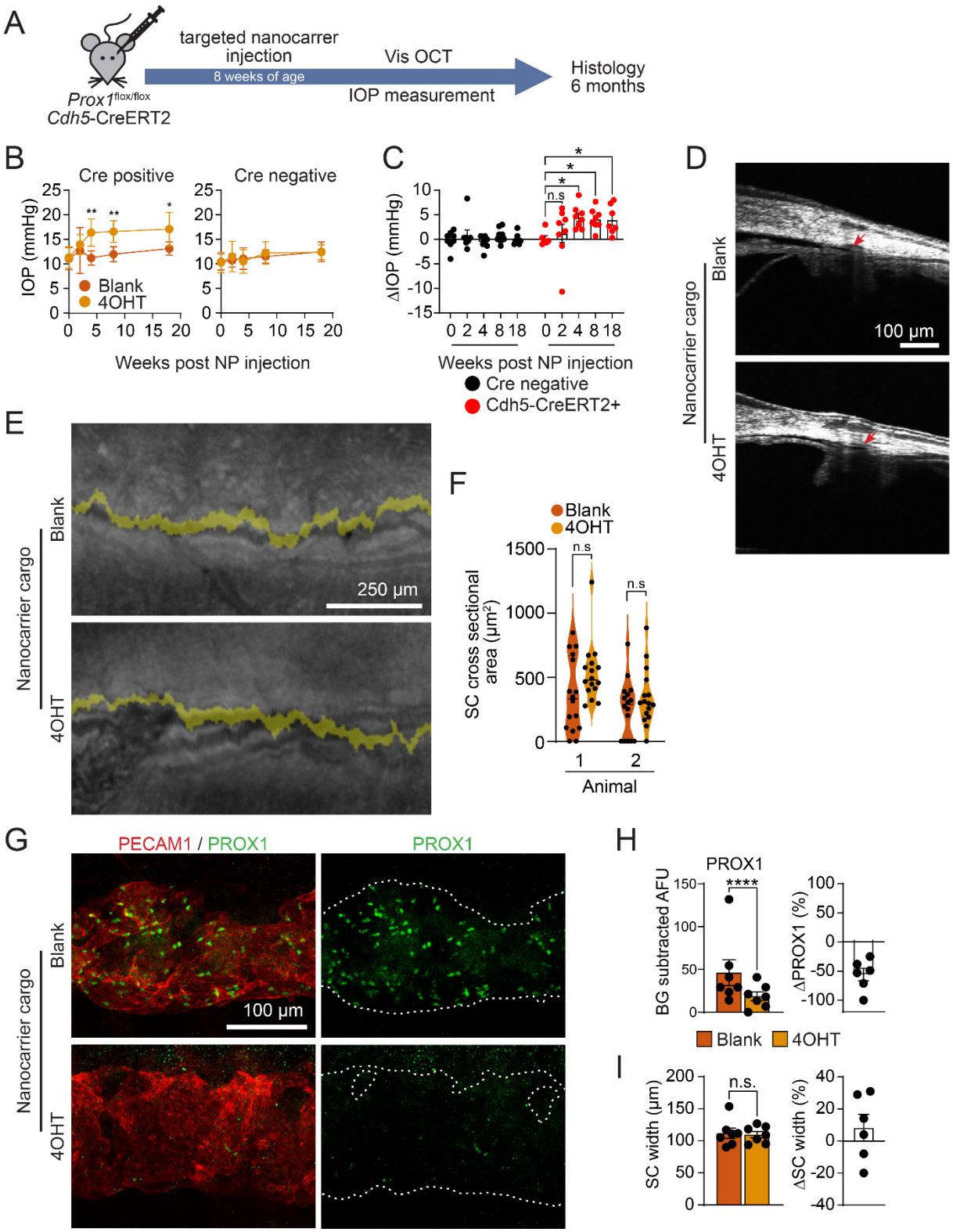
A
targeted nanocarrier injection
8 weeks of age
Vis OCT
IOP measurement
Histology 6 months
Prox1flox/flox
Cdh5-CreERT2
B
Cre positive
Cre negative
IOP (mmHg)
Blank
4OHT
Weeks post NP injection
C
ΔIOP (mmHg)
n.s
Weeks post NP injection
Cre negative
Cdh5-CreERT2+
D
Nanocarrier cargo
Blank
4OHT
100 µm
E
Nanocarrier cargo
Blank
4OHT
250 µm
F
Blank
4OHT
SC cross sectional area (µm²)
n.s
Animal
G
PECAM1 / PROX1
PROX1
Nanocarrier cargo
Blank
4OHT
100 µm
H
PROX1
BG subtracted AFU
****
ΔPROX1 (%)
Blank
4OHT
I
SC width (µm)
n.s.
ΔSC width (%)

999

1000

1001 **Figure 4. Schlemm's canal (SC)-specific *Prox1* deletion leads to ocular hypertension**. (**A**)
1002 Schematic of experimental timeline used for targeted nanocarrier induction of *Prox1* deletion. (**B**,
1003 **C**) 4 weeks after targeted nanocarrier induction, IOP elevation was observed in eyes of
1004 *Prox1*$^{flox/flox}$;*Cdh5*-CreERT2 mice receiving targeted 4OH tamoxifen (4OHT) nanocarriers in
1005 comparison to contralateral eyes receiving identical targeted empty (blank) nanocarriers. IOP
1006 elevation persisted throughout the duration of the experiment. No IOP elevation was seen in
1007 identically treated Cre-negative mice. (Cre+, n = 8, Cre-, n = 8). (**D**) In vivo visible light-OCT
1008 imaging 12 weeks after nanocarrier-mediated *Prox1* deletion revealed no change in canal size on
1009 B-scans, or (**E**) longitudinal reconstructions (pseudo-colored in yellow) of Schlemm's canal. (**F**)
1010 Comparison of luminal area by 16 individual OCT B scans captured around the circumference of
1011 Schlemm's canal showed no difference in canal size between matched 4OHT and blank
1012 nanocarrier-treated eyes of *Cdh5*-CreERT2-positive mice. (**G**) PROX1 expression and canal
1013 morphology were examined in Schlemm's canal flat mounts collected 6 months after nanocarrier
1014 induction by confocal microscopy. Dashed lines in PROX1 panels indicate the outline of
1015 PECAM1-positive Schlemm's canal. (**H**) Compared with contralateral control eyes, PROX1
1016 expression was significantly reduced in eyes treated with 4OHT nanocarriers. (**I**) No significant
1017 change in Schlemm's canal size was observed in 4OHT nanocarrier-treated eyes (n = 6). * $p <$
1018 $0.05$, ** $p < 0.01$, **** $p < 0.0001$ as determined by 2-way ANOVA followed by Bonferroni
1019 posttests (**B**, **C** and **F**) or 2-tailed paired Student's t test (**H** & **I**). Error bars in **B**, **C**, **H**, and **I**
1020 indicate ±SEM, while each point represents an independent biological replicate. Each point in **F**
1021 represents a single measurement captured along the length of Schlemm's canal, while each violin
1022 represents a single eye.

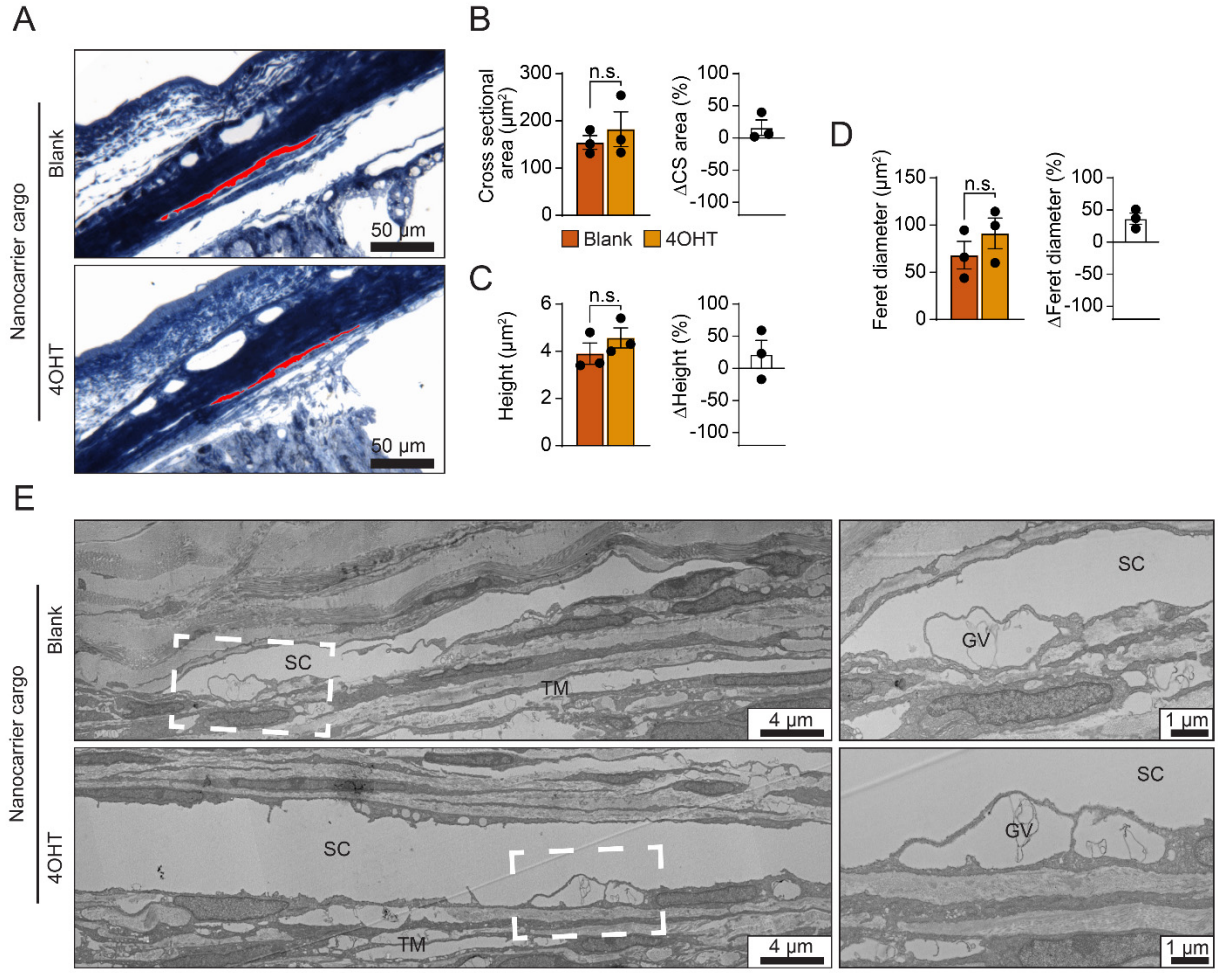


**Figure 5. Light and electron microscopy revealed normal Schlemm's canal (SC) morphology in *Prox1* knockout SC.** (**A**) Representative toluidine blue-stained semithin cross-sections of Schlemm's canal from *Prox1*$^{flox/flox}$; *Cdh5*-CreERT2 eyes 12 weeks after treatment with blank or 4OHT nanocarriers. Semithin sections were imaged by light microscopy and used to measure (**B**) SC cross sectional area, (**C**) canal height (depth) and (**D**) Feret diameter (longest axis; n = 3 pairs of eyes from *Cdh5*-CreERT2-positive nanocarrier-treated animals). Schlemm's canal lumen indicated by red shading. When compared to same-animal contralateral control eyes, no significant difference in canal size or morphology was observed. (**E**) Representative TEM images from the inferior quadrant of matching eyes treated with 4OHT or blank nanocarriers from a *Prox1*$^{flox/flox}$; *Cdh5*-CreERT2 mouse revealed no differences in SC inner wall or juxtacanalicular meshwork morphology 12 weeks after nanocarrier injection. Giant vacuoles (GV) were observed in the inner wall of both 4OHT-treated and contralateral control eyes. Statistical comparisons in **B**-**D** were performed using a Bonferroni-corrected 2-tailed, paired Student's t test. Error bars in **B**, **C**, and **D** indicate ±SEM, while each point represents an independent biological replicate.

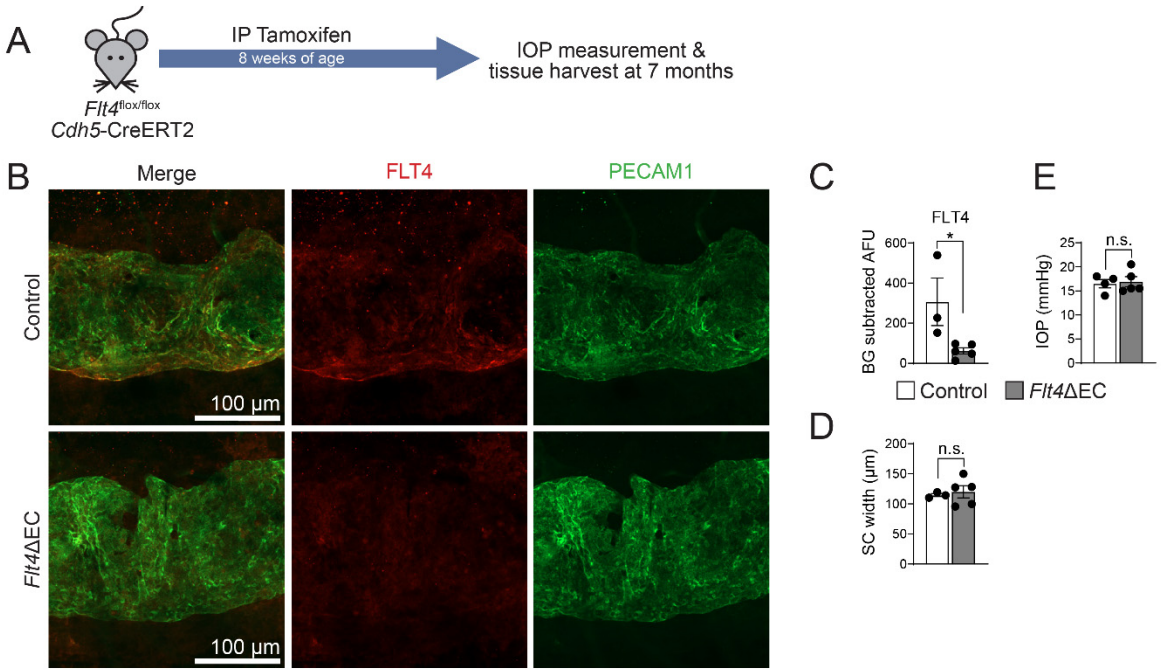


**Figure 6. FLT4 is not required for SC maintenance or IOP homeostasis in adult mice.** (**A**) Experimental outline used for generation and analysis of endothelial-specific *Flt4* knockout mice (*Flt4*ΔEC). (**B**, quantified in **C** & **D**) Confocal microscopy revealed loss of FLT4 immunostaining and similar PECAM1-positive SC size 5 months after *Flt4* deletion. Control, n = 5, *Flt4*ΔEC, n = 3. (**E**) No difference in IOP was observed in between *Flt4*ΔEC mice and control littermates at 7 months of age. Control, n = 5, *Flt4*ΔEC, n = 4. Statistical comparisons in **C**-**E** were performed using a 2-tailed Student's t test. * $p < 0.05$. Error bars indicate ±SEM, while each point represents an independent biological replicate.

**Table 1.** Physicochemical properties of Schlemm's canal targeting nanocarriers

| Nanocarrier | Diameter (nm) | Polydispersity index (PDI) | Zeta potential (ζ) | Encapsulation efficiency |
|---|---|---|---|---|
| 4OHT untargeted | 22.4 ± 4.5 | 0.22 ± 0.09 | -1.98 | 54.78 ± 14.13 |
| 4OHT targeted | 19.1 ± 1.6 | 0.23 ± 0.06 | -1.89 | 47.29 ± 18.00 |
| Blank untargeted* | 17.8 ± 2.0 | 0.14 ± 0.10 | -0.14 | - |
| Blank targeted | 19.4 ± 1.2 | 0.11 ± 0.10 | -1.20 | - |

*Physicochemical characteristics of the different 4OHT targeted and untargeted nanocarriers measured by DLS and Electrophoretic Light Scattering (ELS). Encapsulation efficiency (EE%) of 4OH-tamoxifen was determined by HPLC. Values are shown ±SEM, n = 3 independently prepared replicates per condition. *Blank untargeted nanocarriers were not used in any in vivo experiments but are included here to demonstrate that particle size was unaffected by the addition of the targeting peptide or tamoxifen loading.*

1051

1052

1053